

Modeling reverberation mapping data I: improved geometric and dynamical models and comparison with cross-correlation results

Anna Pancoast¹, Brendon J. Brewer², Tommaso Treu^{1,3}

¹*Department of Physics, University of California, Santa Barbara, CA 93106, USA; pancoast@physics.ucsb.edu*

²*Department of Statistics, The University of Auckland, Private Bag 92019, Auckland 1142, New Zealand*

³*Current address: Physics and Astronomy Building, 430 Portola Plaza, Box 951547, Los Angeles, CA 90095-1547, USA*

17 September 2018

ABSTRACT

We present an improved and expanded simply parameterized phenomenological model of the broad line region (BLR) in active galactic nuclei (AGN) for modeling reverberation mapping data. By modeling reverberation mapping data directly, we can constrain the geometry and dynamics of the BLR and measure the black hole mass without relying on the normalization factor needed in the traditional analysis. For realistic simulated reverberation mapping datasets of high-quality, we can recover the black hole mass to 0.05–0.25 dex uncertainty and distinguish between dynamics dominated by elliptical orbits and inflowing gas. While direct modeling of the integrated emission line light curve allows for measurement of the mean time lag, other details of the geometry of the BLR are better constrained by the full spectroscopic dataset of emission line profiles. We use this improved model of the BLR to explore possible sources of uncertainty in measurements of the time lag using cross-correlation function (CCF) analysis and in measurements of the black hole mass using the virial product. Sampling the range of geometries and dynamics in our model of the BLR suggests that the theoretical uncertainty in black hole masses measured using the virial product is on the order of 0.25 dex. These results support the use of the CCF to measure time lags and the virial product to measure black hole masses when direct modeling techniques cannot be applied, provided the uncertainties associated with the interpretation of the results are taken into account.

Key words: galaxies: active – galaxies: nuclei – methods: statistical

1 INTRODUCTION

While active galactic nuclei (AGN) are thought to be powered by accretion onto super-massive black holes (Lynden-Bell & Rees 1971), much remains unknown about the physical distribution and kinematics of the surrounding gas. A portion of this gas is deep enough in the potential of the black hole that its emission lines are broadened by up to several thousand km/s (Antonucci 1993; Urry & Padovani 1995). At distances from the black hole of $\sim 10^{14} - 10^{16}$ m (Wandel et al. 1999; Kaspi et al. 2000; Bentz et al. 2006, 2013), this so-called broad line region provides a unique probe of AGN physics and the opportunity to measure the mass of the black hole itself, via reverberation mapping (Blandford & McKee 1982; Peterson 1993; Peterson et al. 2004).

Traditionally, the goal of reverberation mapping is to infer a characteristic radius of the BLR by measuring the time lag between changes in the AGN ionizing continuum

(or a proxy such as the optical AGN continuum) and the response of the broad emission line flux. If the time lag is due only to light travel time, then the characteristic radius of the BLR is given by the speed of light c times the time lag τ . The time lag can then be combined with a measure of the velocity of the BLR gas to form a dimensional black hole mass estimate referred to as the virial product, $M_{\text{vir}} = c\tau\Delta v^2/G$, where G is the gravitational constant and Δv is a measure of the width of the broad emission line profile. The virial product is related to the true black hole mass M_{BH} by the virial coefficient f , a dimensionless factor of the order unity. In recent years, the standard practice is to set the average virial coefficient by aligning the $M_{\text{BH}} - \sigma_*$ relations for galaxies with dynamical M_{BH} measurements and galaxies with reverberation mapped black hole mass measurements (Onken et al. 2004; Collin et al. 2006; Woo et al. 2010; Greene et al. 2010; Graham et al. 2011; Park et al. 2012a; Woo et al. 2013; Grier et al. 2013a). The scatter in the $M_{\text{BH}} - \sigma_*$ relation of

~ 0.4 dex (e.g. Park et al. 2012a) indicates that the uncertainty introduced by assuming a single value of f for the full reverberation mapped sample could be comparable to the intrinsic scatter of the $M_{\text{BH}} - \sigma_*$ for quiescent galaxies.

With a new generation of high-quality reverberation mapping datasets (Bentz et al. 2009; Denney et al. 2010; Barth et al. 2011; Grier et al. 2013b), more information has become available to probe the details of the geometry and dynamics of the BLR. In order to exploit this improvement in the data, in the last few years we have been developing a new technique for analyzing reverberation mapping data (Pancoast et al. 2011). The fundamental difference of our approach with respect to previous work is that we aim to fit fully self-consistent models of the BLR geometry and dynamics to the data, rather than trying to infer the so-called transfer function (Blandford & McKee 1982; Horne et al. 1991; Horne 1994; Krolik & Done 1995). In addition to providing quantitative constraints on the geometry and dynamics of the BLR, this direct modeling approach allows us to measure the black hole mass without relying on the virial coefficient f ; instead, the black hole mass is just one of the parameters in our model fit. Previously we applied this direct modeling approach to the $\text{H}\beta$ emission line in two AGNs, Arp 151 (Brewer et al. 2011a) and Mrk 50 (Pancoast et al. 2012), that were observed as part of the Lick AGN Monitoring Projects in 2008 (Walsh et al. 2009; Bentz et al. 2009) and 2011 (Barth et al. 2011), respectively.

In this paper, the first of a series on direct modeling of reverberation mapping data, we introduce an improved and expanded version of our simply parameterized phenomenological model of the BLR to be used with the direct modeling approach. We demonstrate the capabilities of this new model using simulated data and by placing constraints on the uncertainties in traditional cross-correlation function (CCF) analysis. In paper II of this series (Pancoast et al. 2014), we apply the improved BLR model to five AGNs in the LAMP 2008 dataset. The additional model flexibility and increased algorithm efficiency of this new implementation are demonstrated by comparing the results for Arp 151 by Brewer et al. (2011a) to the new results described in paper II; in the latter case the uncertainty in black hole mass is decreased by more than 0.1 dex and it is possible to differentiate between inflow and outflow kinematics.

We begin by presenting a detailed description of the improved BLR model in Section 2. Tests to recover the model parameters using simulated data are presented in Section 3. Comparison of direct modeling results to CCF analysis and constraints on CCF lag uncertainties are given in Section 4. Finally, we give an overview of the main conclusions in Section 5. Throughout this paper, all BLR model parameter values are given in the rest frame of the AGN.

2 THE MODEL

In this section we describe our model of the BLR and the numerical methods we use to explore its parameter space. Our model of the BLR can be applied to any broad emission line, although it has so far only been applied to the $\text{H}\beta$ broad emission line in six AGNs (Brewer et al. 2011a; Pancoast et al. 2012, 2014). The basic methodology of our model is also completely generalizable to any model in which the

geometry and dynamics of the BLR gas can be computed quickly enough to enable a full exploration of the parameter space when comparing with the data.

2.1 Overview

Our goal is to reconstruct the physical structure of the BLR and to measure the mass of the central black hole from reverberation mapping measurements. To achieve this, we describe the possible structure of the BLR by a large number of parameters whose values we infer from the data.

In our model, the BLR is represented by a set of point particles whose positions represent the spatial distribution of broad line emission. If the BLR is really made up of distinct clouds, then each particle could be associated with emission from a BLR cloud, however if the BLR is made up of a smoother distribution of gas, then the particles are just a Monte Carlo approximation of the density field of emission. Each particle in our model is also associated with a velocity that depends upon the mass of the black hole. Our model parameters for the BLR describe the spatial distribution of the particles as well as their individual positions. Additional parameters describe the rule by which velocities are assigned to the particles, as well as the individual velocities themselves. In the present implementation we ignore gravitational interactions or fluid viscosity between particles, and other non-gravitational forces like radiation pressure.

Given a distribution of particles with associated velocities, we can immediately calculate how the BLR would process an input continuum light curve, resulting in an emitted broad line spectrum (e.g. $\text{H}\beta$) that changes (in both total flux and shape) over time. Apart from the conversion from continuum to line flux, we assume that the particles act as mirrors, reflecting the continuum flux towards the observer, where the velocity of the particle determines how far the emission line flux is shifted in wavelength space away from the systematic emission line wavelength at rest with respect to the black hole.

There are three parts to our model of the BLR, which is formulated as an application of Bayesian inference as described in Section 2.2. The first part of the model is the AGN continuum light curve model described in Section 2.3. It is necessary to model the AGN continuum light curve because we need to be able to evaluate the continuum light curve at arbitrary times in order to calculate the broad line spectrum variations predicted by the model. The second part is the “geometry model” (spatial distribution) of the BLR described in Section 2.4, which describes the spatial distribution of the particles that make up the BLR emission. The positions of the particles determine their time lags, which tells us how delayed features in the broad emission line light curve are compared to the continuum light curve. The third part is the “dynamical model” of the BLR described in Section 2.5. This describes the rule by which velocities are assigned to the particles, and allows for scenarios such as near-circular orbits, inflow, or outflow. The component of a particle’s velocity along the line of sight determines which wavelength it affects in the model-predicted broad line spectrum. Once the three parts of our model of the BLR have been specified, we must explore the model parameter space in order to constrain the properties of the BLR given a specific reverberation mapping dataset, as described in Section 2.6.

Finally, we enumerate the limitations of our current model of the BLR and future improvements in Section 2.7.

2.2 Bayesian Inference Framework

We use the formalism of Bayesian statistics to infer the values of our model parameters θ given a reverberation mapping dataset \mathbf{D} . We begin by defining the prior probability distributions of the model parameters, $p(\theta|I)$, which incorporate our initial assumptions about the range of allowed parameter values and depend upon any information I that we have about the problem before we begin. We then assign the probability distribution of the data given a specific set of parameter values $p(\mathbf{D}|\theta, I)$ which tells us how the data and model parameters are related. This term is often called the ‘‘sampling distribution’’, or, once the data is known, the likelihood. Finally, we can combine the prior and likelihood using Bayes’ theorem to obtain the posterior distribution of the model parameters given the data:

$$p(\theta|\mathbf{D}, I) \propto p(\theta|I)p(\mathbf{D}|\theta, I). \quad (1)$$

The normalization constant of the posterior in Equation 1, called the *evidence* or the *marginal likelihood*, is given by

$$p(\mathbf{D}|I) = \int p(\theta|I)p(\mathbf{D}|\theta, I) d^n\theta \quad (2)$$

and is useful for model comparison.

For models with many parameters and in which the posterior distribution is not of a known standard form, it is common to calculate properties of the posterior probability density function (PDF) by generating samples using an algorithm such as Markov Chain Monte Carlo (MCMC). As the number of parameters becomes large and the likelihood function potentially multimodal, however, it can be more efficient to use a more complex algorithm such as Diffusive Nested Sampling (DNS), as described in Section 2.6. DNS has the added benefit that it computes the marginal likelihood, allowing for model selection, unlike most standard MCMC algorithms that only generate posterior samples.

In our inference problem of modeling the BLR, the data consist of two time series. The first is the AGN continuum light curve $\{\mathcal{Y}_i\}$ and its corresponding timestamps and measurement error variances. The second time series is the spectrum of the broad line measured over time, which we will denote by $\{\mathcal{D}_{ij}\}$ (the index i represents the epoch and j the wavelength bin). The overall dataset that enters into Bayes’ theorem is both of these:

$$\mathbf{D} = \{\{\mathcal{Y}_i\}, \{\mathcal{D}_{ij}\}\}. \quad (3)$$

We can split the likelihood function into two parts. The likelihood for the continuum data $\{\mathcal{Y}_i\}$ will be discussed in Section 2.3. For the broad line data, we use the model parameters θ to construct a time series of mock broad emission line spectra $m_{ij}(\theta)$ to compare to the data using a Gaussian likelihood function:

$$p(\mathbf{D}|\theta, I) = \prod_{i,j} \frac{1}{\sigma_{ij}\sqrt{2\pi}} \exp\left[-\frac{1}{2\sigma_{ij}^2} (\mathcal{D}_{ij} - m_{ij}(\theta))^2\right] \quad (4)$$

2.3 Continuum Light Curve Model

Ground-based reverberation mapping campaigns use optical AGN continuum light curves (e.g. in the V or B bands) to track the variability of photons leading to BLR emission, since the true ionizing photons are in the ultraviolet (UV). While it is expected that the UV photons are created in the accretion disk closer to the black hole than the optical photons, the time lag between variability features in the UV and optical is unresolved (Peterson et al. 1991; Korista et al. 1995) or on the order of a day (Collier et al. 1998). For this reason, we do not distinguish between a UV or optical light curve in our model of the BLR, assuming that either light curve is emitted from a point source at the position of the black hole. While the true UV and optical emitting regions in the accretion disk are certainly not point-like, their distance from the black hole is significantly smaller than that of the BLR compared to the uncertainties in the mean BLR radius (e.g. Morgan et al. 2010), suggesting that detailed modeling of the optical or UV emitting region would not be well-constrained by current reverberation mapping datasets. Since our model of the BLR is many particles each reflecting the continuum light curve to the observer with a time lag given by the particle’s distance from the continuum point source, the continuum flux must be computed at arbitrary times within the light curve. Generally, reverberation mapping AGN continuum light curves are too sparsely sampled to resolve intra-day variability using simple linear interpolation between data points. Linear interpolation also incorrectly assumes that there is no uncertainty associated with the interpolation process or the measurements. For these reasons, we model the AGN continuum light curve using a stochastic model of AGN variability, allowing us to evaluate the light curve at arbitrarily small timescales and also to include the continuum light curve model uncertainty into our inference on the properties of the BLR.

We model the continuous AGN continuum light curve $y(t)$ using Gaussian processes (GPs), which allow us to treat the interpolated and extrapolated light curve points as additional parameters in our model, constrained by the data \mathbf{D} . Most of the information about $y(t)$ is, as one would expect, provided by the continuum light curve data $\{\mathcal{Y}_i\}$.

With the GP assumption, the prior distribution for any finite set of interpolated flux values is a multivariate Gaussian:

$$p(\mathbf{y}|\mu_{\text{cont}}, \mathbf{C}) = \frac{1}{\sqrt{(2\pi)^n \det \mathbf{C}}} \times \quad (5)$$

$$\exp\left[-\frac{1}{2}(\mathbf{y} - \mu_{\text{cont}})^T \mathbf{C}^{-1}(\mathbf{y} - \mu_{\text{cont}})\right] \quad (6)$$

where \mathbf{y} are the interpolated continuum light curve points (i.e. evaluations of the function $y(t)$), μ_{cont} is the long-term mean flux value of the light curve, and \mathbf{C} is the covariance matrix. The covariance between any two points in the interpolated continuum light curve depends on the time difference between them, as given by:

$$C(t_1, t_2) = \sigma_{\text{cont}}^2 \exp\left[-\left(\frac{|t_2 - t_1|}{\tau_{\text{cont}}}\right)^{\alpha_{\text{cont}}}\right] \quad (7)$$

where σ_{cont} is the long term standard deviation of the continuum light curve, τ_{cont} is the typical timescale for variations, and α_{cont} is a smoothness parameter between 1 and

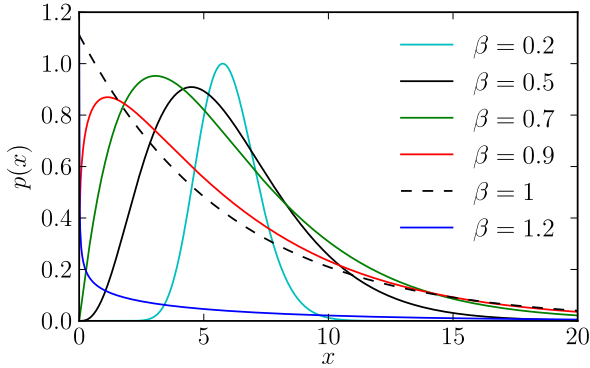


Figure 1. Examples of possible radial profiles for the BLR emission given by the Gamma distribution with $\mu = 6$, $F = 0$, and various values for β . The distributions range from a narrow Gaussian ($\beta < 1$) to an exponential profile ($\beta = 1$) or steeper ($\beta > 1$).

2. Larger values of α_{cont} lead to more covariance between points in the continuum light curve, corresponding to less fluctuations on small timescales. Setting $\alpha_{\text{cont}} = 1$ improves the speed with which the densely sampled continuum light curve can be calculated, as well as increasing the performance of the MCMC¹. For these reasons, we generally set $\alpha_{\text{cont}} = 1$, in which case our Gaussian process model is equivalent to a continuous time first-order autoregressive process (CAR(1)). The CAR(1) model has been found to be a good fit to AGN variability data on similar timescales to those probed by reverberation mapping campaigns (Kelly et al. 2009; Kozłowski et al. 2010; MacLeod et al. 2010; Zu et al. 2011, 2013), although a model that further reduces AGN variability on very short timescales provides a better fit to higher-cadence Kepler data (Mushotzky et al. 2011). We interpolate and extrapolate the AGN continuum light curve data using 1000 points, where the range of points starts before the continuum data (usually by 50% the continuum data range) and extends past the end of both the continuum and line data, whichever is later. Points extrapolated past the ends of the continuum data are only constrained by the general behavior of the interpolated points and thus have very high uncertainty.

2.4 Geometry Model

Once we have a model for the continuum light curve we need a model for the spatial distribution of the particles, which we call the “geometry model”. The geometry model has flexibility in the radial distribution of the particles as well as the angular distribution. In particular we include an opening angle parameter that describes whether the BLR is a disk or sphere and an inclination angle parameter that determines from what angle the observer sees any asymmetries of the BLR. Although this is a purely phenomenological model, it is flexible enough that it should allow us to capture a wide variety of realistic geometries with a moderate number of parameters.

¹ Performance is also increased by parameterising in terms of $\sigma_{\text{cont}}/\sqrt{\tau_{\text{cont}}}$ rather than σ_{cont} itself.

We define the geometry model in two stages. First we consider the radial distribution of the particles, and secondly we define the angular structure.

2.4.1 Radial BLR Distribution

The radial distribution of BLR emission density is described by a shifted gamma distribution. The gamma distribution for a positive variable x is usually written

$$p(x|\alpha, \theta) \propto x^{\alpha-1} \exp\left(-\frac{x}{\theta}\right) \quad (8)$$

where α is the shape parameter and θ is a scale parameter. Our radial distribution is based on a shifted gamma distribution where the lower limit is r_0 instead of zero. Rather than parameterizing the distribution by (α, θ, r_0) , whose interpretations are not straightforward (making priors difficult to assign), we use a different parameterisation in terms of three parameters (μ, β, F) , defined as follows.

$$\mu = r_0 + \alpha\theta \quad (9)$$

$$\beta = \frac{1}{\sqrt{\alpha}} \quad (10)$$

$$F = \frac{r_0}{r_0 + \alpha\theta}. \quad (11)$$

The parameter μ is the mean value of the shifted gamma distribution, β is the standard deviation of the gamma distribution in units of the mean μ when $r_0 = 0$, and F is the fraction of μ from the origin at which the gamma distribution begins (i.e. F is r_0 measured in units of μ). For arbitrary r_0 , the standard deviation of the shifted gamma distribution is:

$$\sigma_r = \mu\beta(1 - F). \quad (12)$$

Finally, we also offset the radial distribution by the Schwarzschild radius, $R_s = 2GM/c^2$, to provide a hard limit to how close a point particle can be to the black hole. For a $10^7 M_\odot$ black hole, $R_s = 0.001$ light days, much smaller than the typical size of the BLR, which is on the order of light days.

The three parameters (μ, β, F) control the radial profile of the particles. To parameterise the actual distances of the particles from the black hole, instead of using the physical distance r , we use a variable g (one for each particle) with a $\text{Gamma}(\beta^{-2}, 1)$ prior. Then the actual distance r of the particle is computed by:

$$r = R_s + \mu F + \mu\beta^2(1 - F)g. \quad (13)$$

The reason for parameterizing in terms of g rather than F is that Metropolis proposals are simpler. For example, a Metropolis move that changes the parameters (μ, β, F) but leaves g fixed will automatically move all of the particles appropriately.

2.4.2 Opening and Inclination Angles

The radial BLR distribution discussed in the previous section is spherically symmetric, however we can break spherical symmetry by introducing a disk opening angle of the BLR. The opening angle is defined as half the angular thickness of the BLR in the angular spherical polar coordinate

perpendicular to the plane of the disk. If the BLR is a sphere then the opening angle is $\pi/2$, and if the BLR is a thin disk then the opening angle approaches zero. Once spherical symmetry has been broken, it is necessary to consider at what angle an observer will view the BLR. The inclination angle is defined as the angle between a face-on BLR geometry and the observer's line of sight, so an edge-on disk would have an inclination angle of $\pi/2$ while a face-on disk would have an inclination angle approaching zero.

To construct a specific BLR geometry, we begin by drawing the radial position for each particle in a flat disk in the x - y plane with the observer located at the positive end of the x -axis. In plane polar coordinates, the radial coordinates r of the point particles are calculated using Equation 13, and the angular coordinates are drawn from a uniform distribution between 0 and 2π . We then puff up this flat disk by the opening angle, first by rotating each particle around the y -axis by some angle between 0 and the opening angle and then by rotating the particle around the z -axis by some angle between 0 and 2π to restore axisymmetry. Next, we rotate all point particles around the y -axis by 90 degrees minus the inclination angle so that an inclination angle of zero corresponds to a face-on BLR geometry. All of the angles used in this process are extra model parameters.

2.4.3 Angular BLR Distribution

We can further add asymmetry by controlling the strength of emission from a given particle using three separate effects:

- (i) The particles are assigned non-uniform weights, depending upon the angle between the observer's line of sight to the central source and a particle's line of sight to the central source. The strength of this effect is controlled by a parameter κ .
- (ii) The parameter γ controls the extent to which the emission is concentrated near the outer edges of the BLR disk at the opening angle.
- (iii) The parameter ξ determines the transparency of the plane of the BLR disk.

The first effect represents anisotropic emission from the point particles. We use first order spherical harmonics to define a weight, W , for each particle that ranges from 0 to 1 and determines what fraction of the continuum flux is reemitted as line flux in the direction of the observer:

$$W(\phi) = \frac{1}{2} + \kappa \cos \phi. \quad (14)$$

The one free parameter is κ , which ranges from -0.5 to 0.5 . Negative values of κ correspond to preferential emission from the far side of the BLR from the observer and positive values correspond to preferential emission from the near side of the BLR. Preferential emission from the far side of the BLR could be physically caused by BLR gas only re-emitting continuum emission back towards the central source due to self-shielding, while preferential emission from the near side of the BLR could be physically caused by the closer BLR gas blocking gas farther away. The angle ϕ is defined to be the angle between the observer's line of sight to the central source and the particle's line of sight to the central source. For $\kappa = -0.5$ and a model where the BLR is made up of spherical balls of gas, this model is equivalent to considering

broad line emission from the area of the spheres illuminated by the central source as viewed by the observer, like lunar phases.

The second effect is parameterized by γ and controls the extent to which BLR emission is concentrated near the outer faces of a disk. This could arise for example if the parts of the BLR closer to the plane of the accretion disk are optically thick. The parameter γ controls preferential emission from the outer faces of the BLR disk by affecting how much the particle positions are moved from an initial flat disk to between zero and the opening angle of a thick disk. The angle for a particle's displacement from a flat to thick disk is given by:

$$\theta = \text{acos}(\cos \theta_o + (1 - \cos \theta_o) \times U^\gamma) \quad (15)$$

where θ_o is the opening angle and U is a random number drawn uniformly between 0 and 1. Larger values of U lead to θ values closer to θ_o , so using U^γ with γ between 1 and 5 concentrates more particles close to the opening angle for $\gamma > 1$.

The third effect represents the possibility for an obscuring medium in the plane of the BLR to partly or completely obscure broad line emission from the back side of the BLR and is parameterized by ξ . Unlike the first effect that depends upon the inclination angle at which an observer views the BLR, ξ is roughly defined as the fraction of particles on the far side of the BLR midplane. In the limit of $\xi \rightarrow 0$, the entire back half of the BLR is obscured, and the BLR geometry could range from half a disk or sphere when $\gamma \sim 1$ to a single cone when $\gamma \sim 5$. In the limit of $\xi \rightarrow 1$, the back half of the BLR is not obscured. Since it is computationally inefficient to throw out particles on the back side of the BLR, we actually just invert their position with respect to the plane of BLR when $\xi < 1$, making the true definition of ξ be the fraction of particles in the back side of the BLR that have *not* been moved to the front side.

2.5 Dynamics Models

In order to make a model spectrum from our geometry of the BLR we must also assign velocities to the particles. We consider three different kinematic components, including bound elliptical orbits and a combination of both bound and unbound inflow or outflow.

2.5.1 Elliptical Orbits

Consider a particle orbiting a point mass at a distance r with velocity $|v| = \sqrt{v_r^2 + v_\phi^2}$, where v_r is the radial velocity and v_ϕ is the tangential velocity in the plane of the orbit and perpendicular to v_r . The tangential velocity in terms of the angular momentum per unit mass of the particle L is given by $v_\phi = L/r$, and the radial velocity can be obtained by considering the energy per unit mass of the particle:

$$E = \frac{1}{2} \left(v_r^2 + \frac{L^2}{r^2} \right) - \frac{GM_{\text{BH}}}{r}. \quad (16)$$

Solving for v_r we obtain:

$$v_r = \pm \sqrt{2 \left(E + \frac{GM_{\text{BH}}}{r} \right) - \frac{L^2}{r^2}}. \quad (17)$$

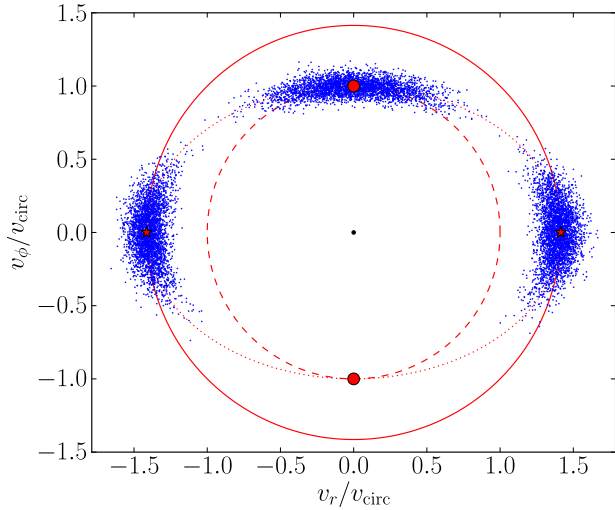


Figure 2. Distributions of radial and tangential velocities, v_r and v_ϕ for the dynamical model. Blue points are particle velocities drawn from Gaussian distributions centered around the point for circular orbits $(v_r, v_\phi) = (0, v_{\text{circ}})$ shown as the upper filled red circle and centered around the points for outflowing and inflowing escape velocity $(v_r, v_\phi) = (\pm\sqrt{2}v_{\text{circ}}, 0)$ shown as filled red stars. The red dotted line denotes the ellipse with semi-minor axis $(v_r, v_\phi) = (0, v_{\text{circ}})$ and semi-major axis $(v_r, v_\phi) = (\sqrt{2}v_{\text{circ}}, 0)$ along which the radial and tangential velocities are drawn. The outer solid red circle at a radius of $|v| = \sqrt{2GM_{\text{BH}}/r}$ denotes the velocity beyond which orbits are unbound. The red dashed circle at a radius of $|v| = \sqrt{GM_{\text{BH}}/r}$ denotes velocities with magnitude of the circular velocity.

For circular orbits, we have the additional constraint that $v_r = 0$ so that the centripetal force of circular motion must equal the gravitational force, giving $v_\phi^2 = GM_{\text{BH}}/r$ or $v_{\text{circ}} = \sqrt{GM_{\text{BH}}/r}$. Thus, the circular orbit solutions are two special points in the $v_r - v_\phi$ plane at $(v_r, v_\phi) = (0, \pm v_{\text{circ}})$.

We consider generalizations of circular orbits to elliptical orbits by considering distributions in v_r and v_ϕ centered around the circular orbit solutions. Such a model allows us to recover circular orbits when the distributions are narrow, but also allows for highly elliptical orbits when the distributions are on the order of v_{circ} . We draw the velocities of the particles from the ellipse in the v_r and v_ϕ plane that has semi-minor axis v_{circ} at $v_r = 0$ and semi-major axis equal to the escape velocity $\sqrt{2}v_{\text{circ}}$ at $v_\phi = 0$, as shown in Figure 2. The reason for drawing velocities from around this ellipse instead of a circle with radius v_{circ} is that the parameter space naturally includes the points at $v_r = \pm\sqrt{2}v_{\text{circ}}$ that correspond to the radial outflowing and inflowing escape velocities. We will discuss these inflowing and outflowing velocity solutions in more detail in Section 2.5.2. Since reverberation mapping measurements cannot distinguish between rotations of the BLR around the line of sight axis, it is only necessary to define the positive v_ϕ side of the $v_r - v_\phi$ plane. The radial and tangential velocities are thus drawn from Gaussian distributions centered at $(v_r, v_\phi) = (0, v_{\text{circ}})$ with standard deviations given by $\sigma_{\rho, \text{circ}}$ and $\sigma_{\Theta, \text{circ}}$, where ρ is the radial coordinate in the $v_r - v_\phi$ plane and Θ is the angular coordinate. Circular orbits are recovered when

$\sigma_{\rho, \text{circ}} \rightarrow 0$ and $\sigma_{\Theta, \text{circ}} \rightarrow 0$, whereas highly elliptical orbits approaching the escape velocity $|v| = \sqrt{2}v_{\text{circ}}$ are obtained when $\sigma_{\rho, \text{circ}} \rightarrow 0.1$ and $\sigma_{\Theta, \text{circ}} \rightarrow 1.0$, the upper limits of their priors.

2.5.2 Inflow and Outflow

In order to include the possibility of substantial unbound outflowing or inflowing gas in the BLR, we allow a variable fraction of the point particles to have elliptical, inflowing, and outflowing orbits. Since we do not expect to find both inflowing and outflowing gas in the BLR in the same spatial location, especially at the velocities assumed by our model, we only allow for inflowing or outflowing particles in addition to elliptical orbits for a specific instance of our model. The fraction of particles with elliptical orbits is given by f_{ellip} , where $1 - f_{\text{ellip}}$ is thus the fraction of particles in either inflowing or outflowing orbits. Whether the orbits are inflowing or outflowing is given by f_{flow} , where values between 0 and 1 and less than 0.5 denote inflow and values greater than 0.5 denote outflow. Inflowing orbits are obtained around values of $(v_r, v_\phi) = (-\sqrt{2}v_{\text{circ}}, 0)$ while outflowing orbits are obtained around values of $(v_r, v_\phi) = (\sqrt{2}v_{\text{circ}}, 0)$.

As for elliptical orbits, we draw the radial and tangential velocities of inflowing or outflowing particles from Gaussian distributions for ρ and Θ , the radial and angular coordinates of the $v_r - v_\phi$ plane. The width of the Gaussian distributions is similarly given by $\sigma_{\rho, \text{radial}}$ and $\sigma_{\Theta, \text{radial}}$, where the widths are the same for both inflowing and outflowing orbits. Since the Gaussian distributions are centered on the points $v_r = \pm\sqrt{2}v_{\text{circ}}$, about half of the inflowing and outflowing particles will actually have bound orbits. In order to allow for completely inflowing and outflowing trajectories, we also allow the distributions centered around $v_r = \pm\sqrt{2}v_{\text{circ}}$ to be rotated by an angle θ_e along the ellipse connecting $v_r = \pm\sqrt{2}v_{\text{circ}}$ to the circular orbit velocities $v_\phi = \pm v_{\text{circ}}$. When $\theta_e = 0$, the inflowing or outflowing orbits are centered around the escape velocities at $v_r = \pm\sqrt{2}v_{\text{circ}}$, while $\theta_e \rightarrow \pi/2$ recovers bound elliptical orbits centered around circular orbits. When $\theta_e \sim \pi/4$, we obtain mostly bound inflowing or outflowing gas.

2.5.3 Macroturbulent Velocities

We also consider macroturbulent velocities of the particles in addition to the velocities from elliptical, inflowing, or outflowing orbits. For each particle, we calculate the magnitude of the turbulent velocity along the observer's line of sight, given by:

$$v_{\text{turb}} = \mathcal{N}(0, \sigma_{\text{turb}})|v_{\text{circ}}| \quad (18)$$

where $\mathcal{N}(0, \sigma_{\text{turb}})$ is a normal distribution centered on zero and with standard deviation σ_{turb} . The magnitude of the turbulent velocity is relative to the magnitude of the velocity of the particle's circular orbit described in Section 2.5.1, given by v_{circ} . We can recover the case with no additional turbulent velocities when $\sigma_{\text{turb}} \rightarrow 0$. We apply the additional macroturbulent velocity to a point particle first by calculating the elliptical, inflowing, or outflowing velocity and then adding v_{turb} . This model for macroturbulent ve-

locities is similar to the one presented by Goad et al. (2012) for the case of a disk with constant opening angle.

2.5.4 Relativistic Effects

As highlighted in Goad et al. (2012), relativistic effects can have a strong influence on the shape of emission line profiles if the BLR gas is sufficiently close to the black hole. We include two simple relativistic effects in the calculation of particle velocities. The first effect is the full relativistic expression for the doppler shift of the broad emission line due to the line of sight velocity of the emitting BLR gas. The second relativistic effect is that of gravitational redshift, which is caused by a photon being emitted from deeper in a gravitational potential well than the observer of the photon. The wavelength shift caused by gravitational redshift depends upon the ratio of the Schwarzschild radius, $R_s = 2GM/c^2$, to the radial distance of the emitting source. Together, the full relativistic expression for doppler shift and the expression for gravitational redshift act to shift the emitted wavelength λ_{emit} of line emission from a particle to the observed wavelength λ_{obs} given by:

$$\lambda_{\text{obs}} = \lambda_{\text{emit}} \frac{\sqrt{\frac{1 + \frac{v}{c}}{1 - \frac{v}{c}}}}{\sqrt{1 - \frac{R_s}{r}}} \quad (19)$$

where the particle has velocity v and radial distance from the black hole r . Since we compare our model broad emission line spectra to the data in wavelength space, we can include the relativistic doppler shift and gravitational redshift in the simulated data by converting the simulated data from velocity to wavelength space using Equation 19.

2.5.5 Narrow Line Emission

In addition to a model of the broad emission line, we must also consider the superimposed narrow emission line from the narrow line region (NLR). Since the NLR is farther from the black hole, the narrow emission line is not expected to reverberate on timescales as short as those for the BLR (e.g. Peterson et al. 2013). We therefore assume that the narrow emission line flux is constant over the duration of a reverberation mapping dataset. We model the narrow emission line component using a Gaussian with line dispersion given by another more isolated narrow emission line profile. For example, to model the narrow component of the $\text{H}\beta$ emission line we use the line dispersion of the narrow $[\text{O III}]\lambda 5007$ emission line, just red-ward of $\text{H}\beta$. Since the width of $[\text{O III}]\lambda 5007$ in a given reverberation mapping dataset is due to both intrinsic line width and instrumental resolution, we use measurements of the intrinsic line width to calculate the instrumental resolution, which is needed to smooth the model spectra. Differences in observing conditions can also change the instrumental resolution as a function of time, so we calculate the line dispersion of the narrow $[\text{O III}]\lambda 5007$ line for each spectrum individually and include the measurements of the line dispersion as free parameters with Gaussian priors given by the line width measurement uncertainties. The intrinsic narrow line width of $[\text{O III}]\lambda 5007$ is also treated as a free parameter with a Gaussian prior

given by the line width measurement uncertainties. For objects where the NLR is not resolved and thus there is no intrinsic line width to the narrow line profile, the width of the narrow emission line directly gives a measurement of the instrumental resolution. Since subtracting narrow emission lines from broad emission lines can introduce significant uncertainty into the spectrum, we model spectra that have not had the narrow emission line subtracted and we include the total flux of the narrow line as an additional free parameter to be constrained by the data.

2.6 Exploring Parameter Space

Once our model of the BLR has been defined, we can explore this high-dimensional parameter space to constrain which parameter values best fit a specific reverberation mapping dataset by measuring the posterior PDFs and correlations between parameters. The full list of all parameters in our BLR model is given in Table 1 along with all of the random numbers used to assign the point particle positions and velocities in Section 2. A probabilistic graphical model (PGM) of the interdependence of the parameters is shown in Figure 3. One way to interpret Figure 3 is as a recipe for making simulated reverberation mapping data:

- (i) Generate a model continuum light curve using Gaussian processes and then
- (ii) sample it to create a realistic continuum light curve.
- (iii) Use BLR geometry and dynamics parameters to generate the positions and velocities of all the particles in the BLR.
- (iv) Finally, use those positions and velocities along with the model continuum light curve to make a simulated time series of broad emission line spectra or integrated broad line fluxes.

As described in Section 2.2, we can explore high-dimensional parameter spaces using an MCMC algorithm. We use the diffusive nested sampling code DNest (Brewer et al. 2011b) due to its ability to explore correlations between parameters efficiently in high dimensional spaces, and because it calculates the Bayesian evidence and thus allows for model selection. DNest works by using multiple walkers to explore parameter space, starting from the prior and gradually adding hard likelihood constraints.

One of the inherent difficulties of fitting real data with a simplified model is that the model is unlikely to match the data perfectly, especially if the error bars on the data are very small. In practice, one often obtains unrealistically precise inferences of the model parameters because the model contains simplifications. However we still expect the model to capture the main features of the structure of the BLR. We account for the systematic uncertainty from using a simple model by inflating the errorbars of the data until only the macroscopic fluctuations in the data are fit by the model. Since we use a Gaussian likelihood function, as discussed in Section 2.2, we can rephrase the inflation of errorbars as an increased weighting of the prior probability compared to the likelihood when calculating the posterior probability. The weighting term is called a ‘‘temperature’’ T , such that $\log(\text{posterior}) \propto \log(\text{prior}) + \log(\text{likelihood})/T$ and hence the inflated errorbars are \sqrt{T} larger than the original errorbars

Table 1. BLR model parameters and their prior probability distributions.

Parameter	Definition	Prior
μ	Mean radius of the BLR radial profile Eq. 9	LogUniform(1.02×10^{-3} light days, Δt_{data})
β	Unit standard deviation of BLR radial profile Eq. 10	Uniform(0, 2)
F	Beginning radius in units of μ of BLR radial profile Eq. 11	Uniform(0, 1)
θ_i	Inclination angle § 2.4.2	Uniform($\cos \theta_i(0, \pi/2)$)
θ_o	Opening angle § 2.4.2	Uniform(0, $\pi/2$)
κ	Cosine illumination function parameter Eq. 14	Uniform(-0.5, 0.5)
γ	Disk edge illumination parameter Eq. 15	Uniform(1, 5)
ξ	Plane transparency fraction § 2.4.3	Uniform(0, 1)
M_{BH}	Black hole mass Eq. 16	LogUniform($2.78 \times 10^4, 1.67 \times 10^9 M_{\odot}$)
f_{ellip}	Fraction of elliptical orbits § 2.5.2	Uniform(0, 1)
f_{flow}	Flag determining inflowing or outflowing orbits § 2.5.2	Uniform(0, 1)
$\sigma_{\rho, \text{circ}}$	Radial standard deviation around circular orbits § 2.5.1	LogUniform(0.001, 0.1)
$\sigma_{\Theta, \text{circ}}$	Angular standard deviation around circular orbits § 2.5.1	LogUniform(0.001, 1.0)
$\sigma_{\rho, \text{radial}}$	Radial standard deviation around radial orbits § 2.5.2	LogUniform(0.001, 0.1)
$\sigma_{\Theta, \text{radial}}$	Angular standard deviation around radial orbits § 2.5.2	LogUniform(0.001, 1.0)
σ_{turb}	Standard deviation of turbulent velocities § 2.5.3	LogUniform(0.001, 0.1)
θ_e	Angle in the $v_{\phi} - v_r$ plane § 2.5.2	Uniform(0, $\pi/2$)

Equation numbers refer to the first equation in which the parameter is used and section numbers refer to those subsections where the parameter is defined. Δt_{data} is the time span between the first and last data point in the reverberation mapping dataset. The prior is designated by the scale in which a parameter is sampled uniformly and by the range (minimum value, maximum value). Uniform(0, 1) denotes a uniform prior distribution between 0 and 1. LogUniform(1, 100) denotes a uniform prior for the log of the parameter, or alternatively, a prior density $p(x) \propto 1/x$, between the parameter values 1 and 100. A log-uniform prior is used for positive parameters whose order of magnitude is unknown.

for a Gaussian likelihood function. Generally higher quality datasets require larger values of T . Another advantage of using nested sampling for the computation is that we can vary the temperature and check the sensitivity of the results without having to repeat the MCMC run.

2.7 Limitations of the Model and Future Improvements

Finally, we discuss some of the limitations of our model of the BLR and discuss improvements to be made in the future. One of the main limitations of our model is the simplified dynamics of the point particles. We ignore the effects of radiation pressure, a force that has a $1/r^2$ dependence like gravity, making it difficult to disentangle from the black hole mass. Unfortunately, this degeneracy of radiation pressure with black hole mass means that black hole masses could be significantly underestimated, and that the degeneracy can only be broken by including external information about the BLR gas density in the model (Marconi et al. 2008, 2009; Netzer 2009; Netzer & Marziani 2010). We also ignore the self-gravity and viscosity of the BLR gas and any interaction it has with the gas in the accretion disk. Finally, we assume that the gas in elliptical orbits is the same gas that could be inflowing or outflowing, when in reality the BLR could have multiple components with different geometries and dynamics.

Another limitation to our model of the BLR is the simplified treatment of radiative transfer, both for the ionizing and broad line photons. We ignore any asymmetry of the ionizing photons except for an optional preference for photons away from the BLR midplane. We also ignore detailed radiative transfer of line photons within the BLR gas, both locally and globally. While we have included two additional

obscurations effects in this new version of the BLR model, transparency of the disk midplane to line photons (ξ) and asymmetry of the ionizing photons away from the disk midplane (γ), these are simplifications of what is most likely an inherently complicated problem.

Some of these limitations can be at least partially solved in future models of the BLR. For example, CLOUDY models constrain the direction in which line photons are emitted from individual clouds of BLR gas, as well as the emissivity and responsivity of line emission as a function of radius (e.g. Ferland et al. 1998, 2013). Using a table of pre-computed values from CLOUDY would not only provide a more physically-detailed local opacity to our model, but would also constrain the radial distribution of broad line emitting gas. By modeling the BLR using multiple broad emission lines simultaneously, we can also start to place constraints on the underlying distribution of gas density.

Recently Li et al. (2013) developed an independent code to model reverberation mapping data using a geometry model of the BLR based on the model of Pancoast et al. (2011). They include additional flexibility in their model by allowing for non-linear response of the broad emission lines to incident continuum radiation. While the average emission line response of their sample is close to linear, they find that individual AGNs can have non-linear response, suggesting that this effect may be important to include in future implementations of our modeling code.

Another improvement that could be made to our model is better treatment of the dynamics. One option could be to include separate geometries for each dynamical component, for example a thin disk of gas in elliptical orbits with a cone of outflowing gas. We could also improve our treatment of outflows to include the detailed dynamics found in simulations of disk winds or complex models of outflows. For example, instead of assuming that outflowing gas has

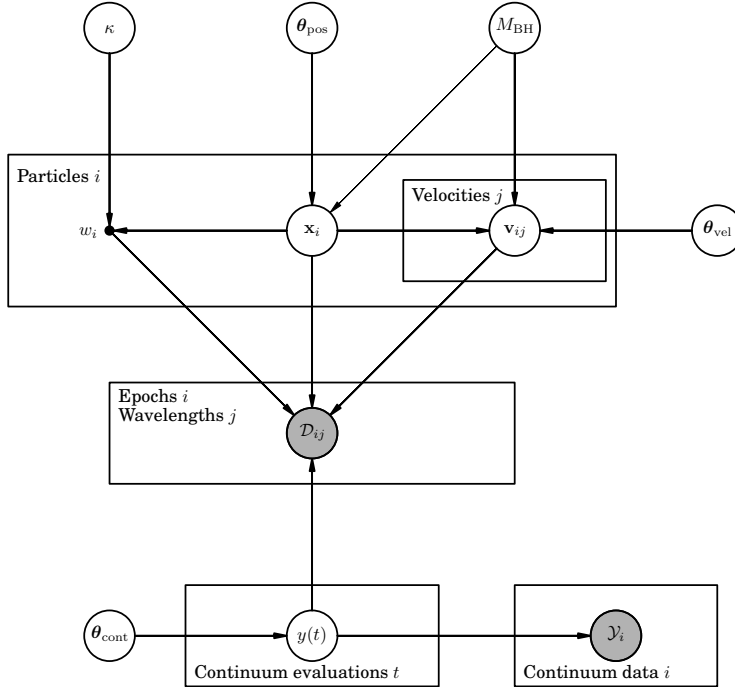


Figure 3. A probabilistic graphical model of the parameters and their influence on simulated reverberation data created by the BLR model. Each unshaded node represents a parameter (e.g. M_{BH}) or continuum hyperparameter (e.g. θ_{cont}) in the model and each shaded node represents a data value (e.g. \mathcal{D}_{ij}). Arrays of parameters are represented with a box, which can be thought of as a for loop. The arrows represent dependence between two nodes, where the arrow between M_{BH} and \mathbf{x}_i corresponds to a weak dependency due to the minimum BLR radius being set by the Schwarzschild radius. The geometry model parameters, which determine the positions of the particles \mathbf{x}_i , include κ and θ_{pos} , a vector of the remaining geometry model parameters given in Table 1: μ , β , F , θ_i , θ_o , γ , and ξ . The dynamics model parameters, which determine the velocities of the particles \mathbf{v}_{ij} , include M_{BH} and θ_{vel} , a vector of the remaining dynamics model parameters given in Table 1: f_{ellip} , f_{flow} , $\sigma_{\rho, \text{circ}}$, $\sigma_{\Theta, \text{circ}}$, $\sigma_{\rho, \text{radial}}$, $\sigma_{\Theta, \text{radial}}$, σ_{turb} , and θ_e . The continuum hyperparameters in vector θ_{cont} include μ_{cont} , σ_{cont} , τ_{cont} , and α_{cont} . This figure was made using daft-pgm.org.

mainly radial trajectories at or near the escape velocity of its present position, we could consider the more complicated case where the gas is accelerated to velocities on the order of the escape velocity and where the escape velocity is defined at an initial wind launching radius instead of the current position of the gas (e.g. Castor et al. 1975; Proga 1999).

Finally, breathing of the BLR may play an important role in determining the response of emission line flux as a function of time (see Korista & Goad 2004, and references therein). Breathing of the BLR is where BLR emission comes from gas farther from or closer to the central engine based on increases or decreases in the ionizing luminosity, respectively. If the mean radius of the BLR changes substantially over the course of a reverberation mapping campaign, then this could have a noticeable effect on the measured time lag and the results from direct modeling analysis.

3 TESTS WITH SIMULATED DATA AND ARP 151

We demonstrate the capabilities of our improved model of the BLR and direct modeling code by recovering the model parameters for two simulated reverberation mapping

datasets. By modeling the time series of emission line profiles using a geometry and dynamical model of the BLR as well as modeling the integrated emission line light curve using a geometry model of the BLR, we illustrate the benefits of a full spectroscopic dataset.

3.1 The simulated datasets

In order to generate realistic simulated reverberation mapping datasets, we use the LAMP 2008 dataset of $\text{H}\beta$ emission for Arp 151 (Walsh et al. 2009; Bentz et al. 2009) to determine the sampling cadence, flux errors, instrumental smoothing, and approximate scale of the BLR. The Arp 151 dataset includes a B -band continuum light curve and a time series of $\text{H}\beta$ emission line profiles, where the broad and narrow $\text{H}\beta$ flux is isolated from the spectrum using spectral decomposition techniques as described by Park et al. (2012b). As described in Section 2.6, the simulated datasets are created by first generating a model of the Arp 151 continuum light curve using Gaussian processes and sampling that model continuum light curve with the same cadence as for Arp 151. We then add Gaussian noise to the continuum light curve using the error vector of the Arp 151 light curve. Next we set fixed the BLR geometry and dynamics

Table 2. Geometry and dynamics true parameter values of simulated spectral datasets and inferred geometry and dynamics posterior median parameter values and 68% confidence intervals.

Geometry Model Parameter	Simulated Data 1 (True)	Simulated Data 1 (Inferred)	Simulated Data 2 (True)	Simulated Data 2 (Inferred)
r_{mean} (light days)	4.0	$4.19^{+0.21}_{-0.21}$	4.0	$3.54^{+0.44}_{-0.35}$
r_{min} (light days)	1.0	$0.85^{+0.18}_{-0.26}$	1.0	$0.89^{+0.22}_{-0.19}$
σ_r (light days)	3.0	$3.23^{+0.30}_{-0.25}$	2.4	$2.39^{+0.40}_{-0.24}$
τ_{mean} (days)	3.62	$3.59^{+0.15}_{-0.15}$	3.39	$3.30^{+0.18}_{-0.15}$
β	1.0	$0.97^{+0.09}_{-0.09}$	0.8	$0.92^{+0.09}_{-0.11}$
θ_o (degrees)	40	$49.0^{+8.4}_{-7.6}$	30	$27.3^{+11.0}_{-8.6}$
θ_i (degrees)	20	$20.2^{+2.7}_{-3.3}$	20	$22.8^{+10.0}_{-6.7}$
κ	-0.4	$-0.31^{+0.09}_{-0.09}$	-0.4	$-0.16^{+0.31}_{-0.24}$
γ	5.0	$2.73^{+1.29}_{-1.19}$	5.0	$3.50^{+1.02}_{-1.86}$
ξ	0.3	$0.31^{+0.10}_{-0.08}$	0.1	$0.53^{+0.37}_{-0.32}$
Dynamical Model Parameter	Simulated Data 1 (True)	Simulated Data 1 (Inferred)	Simulated Data 2 (True)	Simulated Data 2 (Inferred)
$\log_{10}(M_{\text{BH}}/M_{\odot})$	6.5	$6.42^{+0.06}_{-0.05}$	6.5	$6.48^{+0.08}_{-0.26}$
f_{ellip}	0.0	$0.07^{+0.05}_{-0.04}$	1.0	$0.84^{+0.12}_{-0.50}$
f_{flow}	0.0	$0.25^{+0.18}_{-0.17}$	–	$0.32^{+0.28}_{-0.22}$
θ_e (degrees)	0.0	$7.9^{+7.1}_{-5.0}$	–	$70.2^{+16.7}_{-38.6}$
σ_{turb}	0.0	$0.024^{+0.055}_{-0.021}$	0.0	$0.009^{+0.026}_{-0.007}$

The columns with (True) give the true parameter values for the simulated datasets and the columns with (Inferred) give the inferred parameter values and their uncertainties. True parameter values with – are unimportant for that specific simulated dataset.

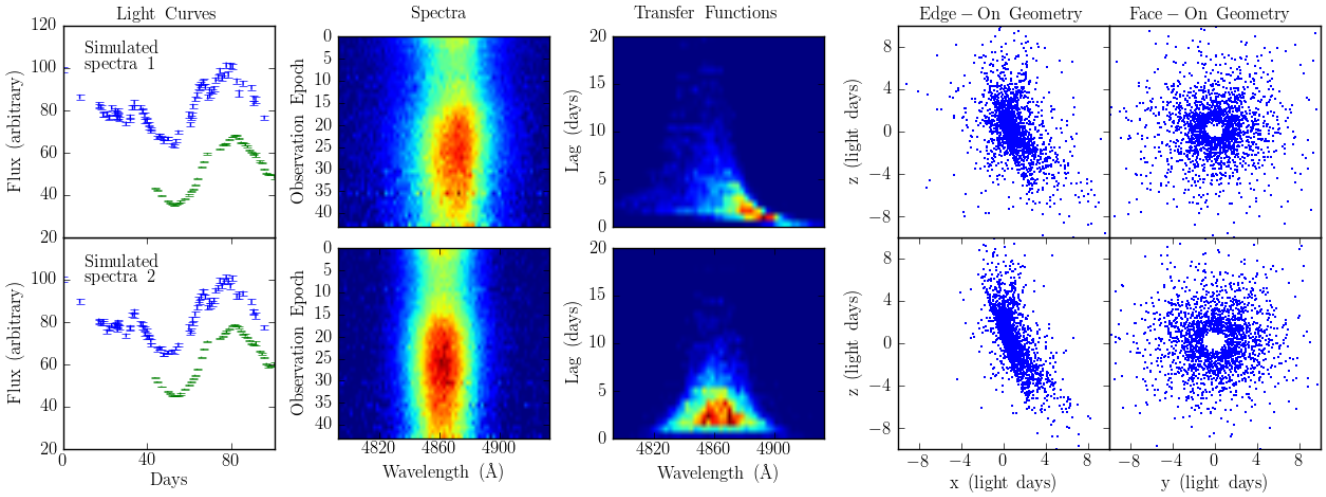


Figure 4. Simulated spectral time series 1 (top row) and 2 (bottom row). First (leftmost) column shows the integrated line light curve in green and the continuum light curve in blue. Second column shows the spectral time series over the wavelength range of the emission line as a function of time series epoch. Third column shows the transfer function as a function of time lag and wavelength. Fourth and fifth columns show the edge-on and face-on views, respectively, of the BLR geometries for each simulated dataset (the observer views the origin from the positive x-axis).

model parameters to the values found in Table 2 and sample the $H\beta$ emission line profile at the times given by the Arp 151 spectral dataset. Finally, we add Gaussian noise to the model spectra based on the spectral errors in the Arp 151 dataset. In order to account for the fact that real reverberation mapping datasets are likely more complicated than our model of the BLR assumes, we inflate the spectral errors and added Gaussian noise on the simulated dataset by a factor

of three compared to the Arp 151 dataset, to obtain more realistic uncertainties on the inferred model parameters. To reduce numerical noise in the simulated spectra to less than the uncertainty in the spectral fluxes, we use 2000 particles and assign each one ten independent velocity values. The width of the narrow line component of $H\beta$ is modeled using the line dispersion of the narrow $[\text{O III}]\lambda 5007$ emission line from the Arp 151 dataset, calculated for each epoch of

spectroscopy. The instrumental resolution is then measured by comparing the measured line dispersion for $[\text{O III}]\lambda 5007$ with its intrinsic line width as calculated by Whittle (1992).

The simulated datasets are based on the geometry and dynamics inferred for the LAMP 2008 dataset in paper II as shown in Table 2, with small mean radii for the BLR of 4 light days, close to exponential radial profiles with $\beta \sim 1$, substantial width to the BLR of $\sim 2 - 3$ light days, thick disks with opening angles of $30 - 40$ degrees, close to face-on inclination angles of 20 degrees, preferential emission from the far side of the BLR ($\kappa = -0.4$) and the edges of the disk ($\gamma = 5$), and mostly opaque mid-planes ($\xi = 0.1 - 0.3$). The black hole masses are also chosen to be similar to the LAMP 2008 sample with $M_{\text{BH}} = 10^{6.5} M_{\odot}$ and each of the simulated datasets is dominated by either elliptical orbits or inflowing orbits. The differences between the simulated datasets can also be easily seen in Figure 4, which shows not only the continuum, line, and spectral timeseries, but also the transfer functions and geometries of the BLR. The simulated spectral datasets consist of the following:

- (i) A thick, wide disk with an exponential profile and dynamics dominated by inflowing orbits.
- (ii) A thinner, narrower disk, with a radial profile between a Gaussian and exponential and dynamics dominated by elliptical orbits.

The continuum light curve interpolation using Gaussian processes is also held constant for all three simulated datasets, although the random noise added to each realistically sampled continuum light curve is different.

While not an issue for simulated emission line profiles, real reverberation mapping data must contend with ambiguity in multiple spectral components overlying the broad emission line profile. For example, with $\text{H}\beta$ we not only have possible overlap of the red wing with the narrow $[\text{O III}]$ emission lines and the blue wing with He II , but there may also be substantial overlap with Fe II broad line emission. Blending between multiple broad components is especially important to disentangle because the different broad emission lines will be generated in BLR gas at different radii from the black hole and blending could confuse the dynamical modeling results. In order to isolate any single broad emission line profile, it is necessary to apply a method of spectral decomposition that will remove most of the ambiguity in overlapping spectral components.

3.2 Recovery of model parameters: spectral datasets

As a first test of our direct modeling code and BLR model, we attempt to recover the true parameter values of the two simulated spectral datasets described in Section 3.1. We assume the same instrumental resolutions as a function of time that are used to generate the simulated datasets and use 2000 particles and assign ten independent velocities to each one. Since we add Gaussian noise to the simulated datasets, we do not expect to recover every parameter of the BLR exactly. In addition, certain BLR geometries and dynamics make it difficult to constrain certain parameters. For example, when the majority of particles are in elliptical orbits, the fraction of particles in inflowing or outflowing orbits may not be well constrained. Or, a nearly face-on very thin disk will

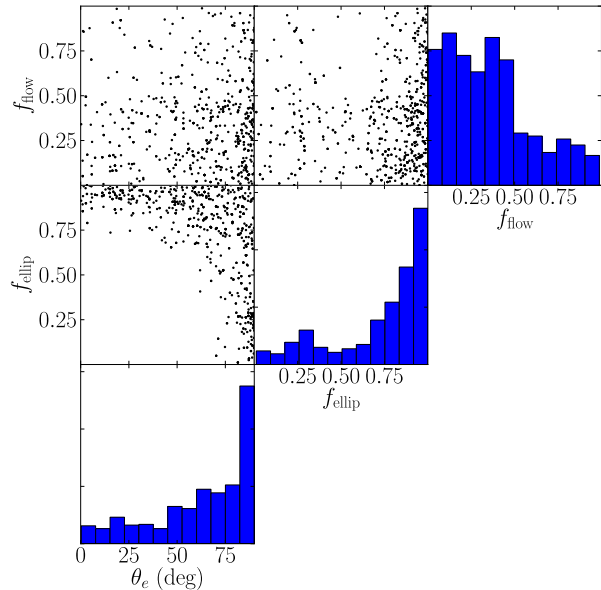


Figure 7. Marginal posterior PDFs and correlations between parameters for simulated dataset 2, including the fraction of elliptical orbits (f_{ellip}), the flag determining inflowing or outflowing orbits (f_{flow}), and the angle in the $v_{\phi} - v_r$ plane (θ_e).

make it difficult to constrain the parameters κ , γ , and ξ since these parameters affect the relative line emission throughout the height of the very thin disk in this case.

The inferred posterior PDFs for the BLR geometry and dynamics model parameters are shown in Figures 5 and 6 for simulated datasets 1 and 2, respectively. The true parameter values for the simulated datasets are shown by vertical red dashed lines for comparison, and in the cases where the true parameter value does not matter (e.g. when the dynamics are entirely dominated by elliptical orbits so there is no true value of f_{flow}) no red line is given. Overall, the modeling code is able to recover the true parameter values to within reasonable uncertainties, as listed in Table 2. Specifically, we constrain the mean radius of the BLR to within 0.5 light days uncertainty, the mean time lag to within 0.2 days uncertainty, and the inclination and opening angles to within ~ 10 degrees. The geometry parameters that add asymmetry to the BLR are more difficult to constrain, with κ and ξ well constrained for simulated dataset 1 while neither κ , γ , nor ξ are well-determined for simulated dataset 2.

We also constrain $\log_{10}(M_{\text{BH}}/M_{\odot})$ to 0.05 – 0.25 dex uncertainty, where the variation comes mainly from larger correlated uncertainties with the inclination and opening angles for simulated dataset 2. The dynamics are also well-recovered for both simulated datasets, with a clear preference for inflow in simulated dataset 1 and for elliptical orbits centered around the circular orbit values in simulated dataset 2. A clearer picture of the preference for elliptical orbits for simulated dataset 2 can be seen in Figure 7, which shows the correlations between f_{ellip} , f_{flow} , and θ_e . Specifically, for values of θ_e approaching 90 degrees, the distribution of inflowing or outflowing orbits becomes identical

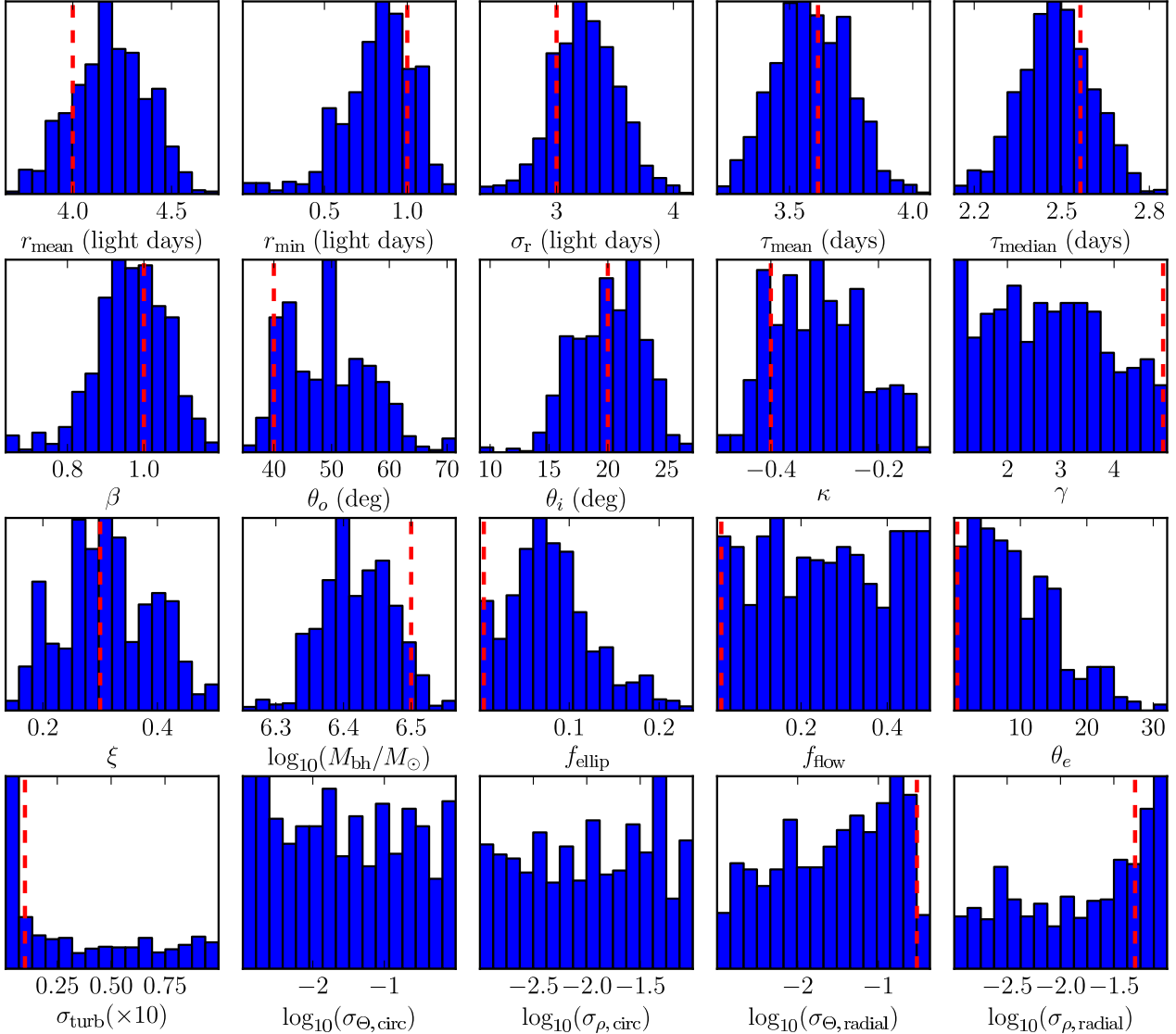


Figure 5. Inferred model parameters for simulated spectral dataset 1. The true parameter values are given by the vertical dashed red lines for those cases where the true value affects the shape of the simulated spectral dataset.

to the distribution for elliptical orbits centered around the circular orbit value in the $v_\phi - v_r$ plane. This means that when $\theta_e \sim 90$ degrees, although f_{ellip} and f_{flow} are mostly unconstrained, the velocity distribution for the particles is very similar to that of $f_{\text{ellip}} \sim 1$.

In general, these two simulated spectral datasets show that we can expect to obtain substantial constraints on the geometry and dynamics of the BLR for reverberation mapping datasets similar in quality to LAMP 2008. The potential constraints on the black hole mass are also promising, although they depend upon the geometry of the BLR, specifically the precision with which we can measure the inclination and opening angles.

3.3 Recovery of model parameters: integrated line datasets

For those cases where a full spectroscopic reverberation mapping dataset is not available, we can apply a geometry-only model of the BLR and reproduce integrated emission line flux light curves. We test whether this approach provides constraints on the geometry of the BLR that are comparable to the full geometry plus dynamical modeling problem using the simulated datasets described in Section 3.1 and shown in the left panel of Figure 4.

We find that the mean time lag and mean radius are well constrained with geometry-only modeling. The mean and median time lag inferred for each simulated dataset are given in Table 3, along with the true mean and median lag values and the value measured by CCF analysis. The inferred mean time lag is not only accurate, but the inferred uncertainty in the mean time lag through geometry-only modeling of

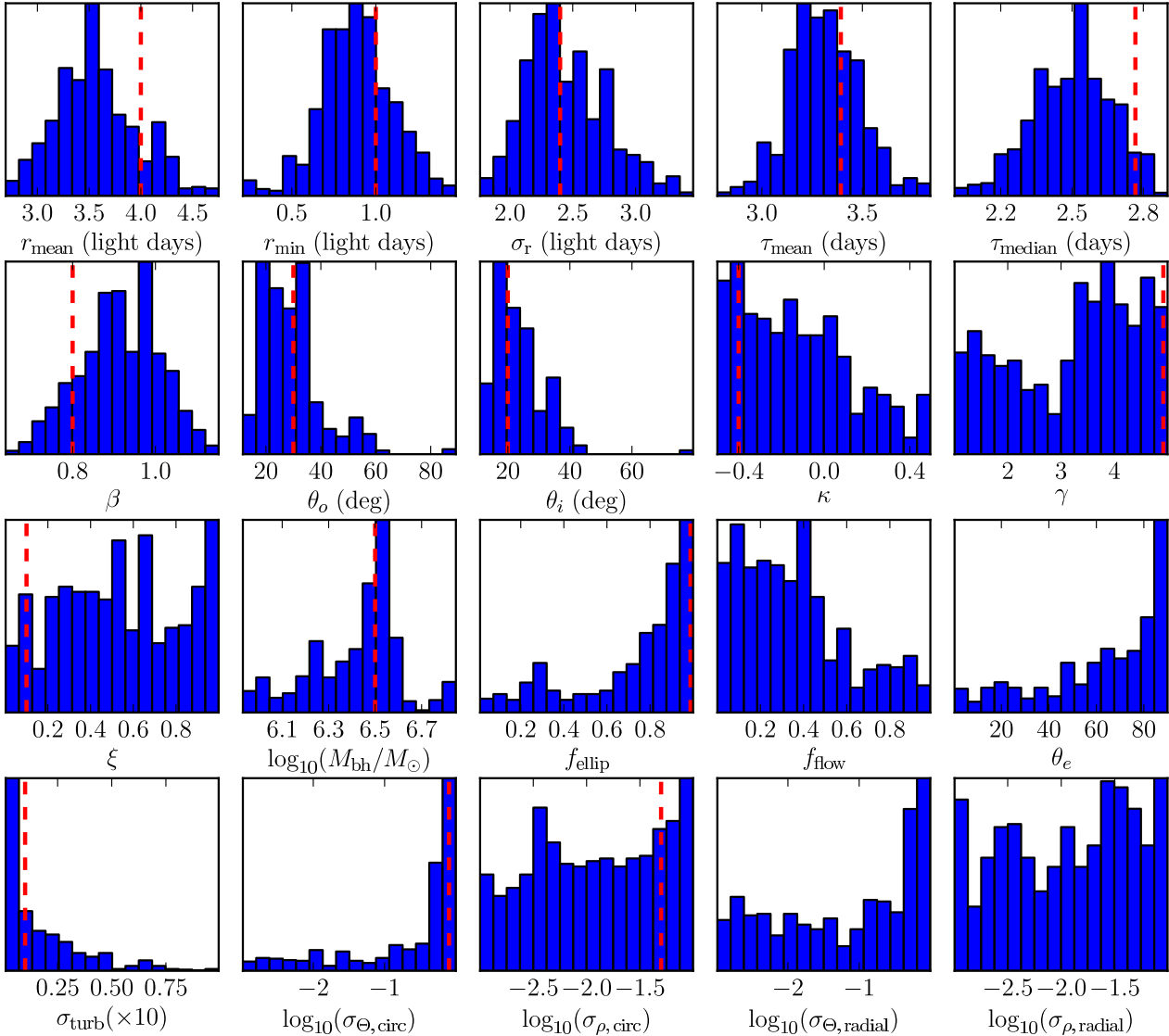


Figure 6. The same as Figure 5 for simulated spectral dataset 2.

~ 0.25 days is almost half as large as for the CCF time lag. This shows that geometry-only modeling is a promising tool for measuring time lags. The mean radius is inferred with slightly larger uncertainties to be $3.58^{+1.18}_{-0.97}$ light days for simulated dataset 1 and $2.90^{+0.97}_{-0.24}$ for simulated dataset 2, while the true mean radius is 4 light days.

Unfortunately the other geometry model parameters are not as well constrained. The parameters γ and ξ are completely unconstrained for both of the simulated datasets, and θ_o , θ_i , β , F , and κ are mostly unconstrained. Generally there is a slight preference for a specific value of θ_o , θ_i , β , F , and κ , but none or almost none of the parameter space is ruled out. These results for geometry-only modeling suggest that a full spectroscopic reverberation mapping dataset is needed to constrain the geometry of the BLR, since otherwise there are too many degeneracies between model parameters to infer anything other than the mean time lag and mean radius consistently.

Table 3. Comparison of BLR geometry modeling, JAVELIN, and CCF lag measurements.

Lag (days)	Sim Data 1	Sim Data 2
True mean lag	3.62	3.39
True median lag	2.56	2.77
τ_{mean}	$3.36^{+0.20}_{-0.15}$	$3.29^{+0.23}_{-0.17}$
τ_{median}	$2.61^{+0.25}_{-0.21}$	$3.10^{+0.17}_{-0.18}$
τ_{JAVELIN}	$2.94^{+0.13}_{-0.12}$	$3.21^{+0.13}_{-0.14}$
τ_{cen}	$3.70^{+0.50}_{-0.48}$	$3.62^{+0.56}_{-0.40}$

τ_{mean} and τ_{median} are the mean and median time lags inferred from BLR geometry modeling, τ_{JAVELIN} is the time lag measured by JAVELIN, and τ_{cen} is the center-of-mass lag measured from the CCF.

3.4 Comparison with JAVELIN

Recently another method has been developed for measuring the time lag in reverberation mapping data using integrated emission line light curves by Zu et al. (2011). This method has been implemented in an open-source code called JAVELIN written in Python.² JAVELIN works by using a top-hat transfer function with two parameters, a mean lag and a width of the top hat. The continuum light curve in JAVELIN is interpolated using a CAR(1) model, which is equivalent to the continuum model implemented here. The parameter space of the continuum light curve and transfer function models is sampled using MCMC, providing posterior PDFs for the model parameter values.

We can compare recovery of the time lag using BLR geometry modeling of integrated emission line light curves to the results from JAVELIN. For simulated dataset 1, we measure a mean lag of $\tau_{\text{JAVELIN}} = 2.94^{+0.13}_{-0.12}$ days and a mean width of the top-hat transfer function of $w = 7.33^{+0.26}_{-0.30}$ days using JAVELIN. This can be compared to the true mean lag of 3.62 days and the true median lag of 2.56 days for simulated dataset 1 to see that the mean lag measured by JAVELIN is between the true mean and median lags. For simulated dataset 2, we measure $\tau_{\text{JAVELIN}} = 3.21^{+0.13}_{-0.14}$ days and $w = 5.26^{+0.82}_{-0.63}$ days. Again, the mean lag measured by JAVELIN is between the true mean lag of 3.39 days and the true median time lag of 2.77 days, although closer to the mean lag. The tendency for the time lag measured by JAVELIN to fall closer to the true mean or median lag is due to the shape of the transfer function; in very asymmetric transfer functions, the mean and median time lag are increasingly discrepant, with JAVELIN more sensitive to the true median time lag for very asymmetric transfer functions.

While the tendency of JAVELIN to measure a time lag ranging between the true mean and median time lags may appear to complicate its interpretation, an uncertainty of ~ 1 day from the difference between the true mean and median lags is comparable to the uncertainty introduced by additional assumptions, as discussed in Section 4, when using time lag measurements to estimate the mean radius of the BLR or to measure the black hole mass. These comparisons suggest that JAVELIN is an excellent resource for measuring the time lag even if the JAVELIN lag uncertainties do not reflect the uncertainty introduced by asymmetric transfer functions. However, to constrain more than the time lag, more flexible modeling of the transfer function must be done.

In comparison, the CCF lag measurements for the two simulated datasets agree with the true mean lag values due to larger uncertainties. The CCF lag measurements do not agree more closely with the true median lag values than with the true mean lag values for more asymmetric transfer functions, as for JAVELIN lags. The quoted error bars on the CCF lag values, τ_{cen} , in Table 3 are calculated by drawing a random subset of the line and continuum light curves points, with the same number of random draws as the original light curves. For points in the light curves that are drawn N times, the flux error is reduced by \sqrt{N} . Finally, the randomly drawn light curve fluxes are modified by adding random Gaussian noise given by the flux errors.

This is similar to the “flux randomization”/“random subset selection” (FR/RSS) approach described in Peterson et al. (1998) except the FR/RSS approach throws out any redundant points in the light curve instead of reducing the flux errors by \sqrt{N} , resulting in slightly larger uncertainties in the CCF lag. The CCF time lag is measured for 1000 iterations of this sequence and we quote the median and 68% confidence intervals of the CCF time lag distributions. For the two simulated datasets tested here with data quality comparable to the LAMP 2008 dataset for Arp 151 (Bentz et al. 2009), the error bars are ~ 0.5 days, or $\sim 14\%$ the value of τ_{cen} . This comparison suggests that while CCF analysis may not give the most precise measurement of the mean or median time lag, the CCF lag uncertainties likely include much of the systematic uncertainties from an unknown transfer function.

Finally, we also consider the effects of detrending the light curves before calculating the CCF lag. Detrending can improve the shape of the CCF when there are strong long-term trends that can be removed by subtracting a linear fit to the light curves (Welsh 1999). Since our simulated data do not contain strong long-term trends, detrending the light curves should have minimal impact on the measured CCF lags. We confirm this by subtracting a linear fit to the simulated continuum light curves from both the continuum and line light curves. Due to the difference in length between the continuum and line light curves, fitting the continuum and line light curves with linear fits separately destroys the correlation between the light curves. When we use a linear fit to the continuum light curve to detrend both light curves we obtain CCF lag measurements for simulated dataset 1 of $\tau_{\text{cen}} = 3.37^{+0.48}_{-0.37}$ days and for simulated dataset 2 of $\tau_{\text{cen}} = 3.38^{+0.47}_{-0.37}$ days, which agree to within the uncertainties with the un-detrended CCF lag values.

3.5 Dynamical modeling without a full spectral dataset

As shown in Section 3.3, a spectroscopic dataset offers substantially more information about the BLR for direct modeling. Here we explore an intermediate case, where the available data consist of the usual continuum light curve, an integrated emission line light curve, and a mean spectrum. Since the mean spectrum contains some information about the kinematics of the BLR, we can model this dataset using the fully dynamical model of the BLR. However, with only the mean spectrum, this dataset cannot constrain the time lag as a function of velocity or wavelength, as possible for a full spectroscopic dataset.

In order to provide a test of this intermediate dataset case that is as realistic as possible, we use the LAMP 2008 dataset for Arp 151. A description of the dataset can be found in paper II. In the analysis of this test, we focus on the differences in inferred parameter values between this test and the full dynamical modeling results presented in paper II. In general, the modeling results for the full spectroscopic dataset and for the intermediate dataset are fully consistent, but the uncertainty on the inferred model parameter values is much larger for the intermediate dataset. For example, the black hole mass is inferred to have a posterior PDF with a long tail at high masses, giving $\log_{10}(M_{\text{BH}}/M_{\odot}) = 6.74^{+0.66}_{-0.13}$ compared to the value from Paper II of $\log_{10}(M_{\text{BH}}/M_{\odot}) =$

² Download JAVELIN here: <https://bitbucket.org/nye17/javelin>

$6.62^{+0.10}_{-0.13}$. Similarly, the uncertainty in θ_i , θ_o , and κ is larger by at least a factor of 3, the uncertainty in ξ is larger by at least a factor of two, and γ is completely undetermined for the intermediate dataset. The two marginally consistent results are the mean radius and mean lag, which are both substantially larger for the intermediate dataset and have uncertainties at least 10 times larger than for the full spectroscopic dataset. This is due to a preference for $\beta \rightarrow 2$, corresponding to heavy-tailed radial distributions where the median radius and median lag are more consistent measurements of the characteristic size of the BLR. Overall, this test suggests that considerable information about the BLR can be inferred from the mean line profile, but the constraints on BLR geometry and dynamics parameters are significantly better when the full spectroscopic dataset is used. Finally, while this intermediate dataset allows for measurement of the black hole mass, it cannot be constrained to less than the ~ 0.4 dex scatter in the f factor due to a tail in the posterior PDF at high masses.

4 COMPARISON WITH CROSS-CORRELATION ANALYSIS

We can compare the results of direct modeling to the standard reverberation mapping analysis of using the cross-correlation function (CCF) to measure time lags and the dispersion or FWHM of the broad emission line to measure a characteristic velocity of the BLR. In addition to providing a sanity check on our direct modeling results, such a comparison allows us to explore some of the uncertainties involved in standard reverberation mapping analysis. First, we consider the time lag traditionally measured using the CCF, how it compares to a measurement of the mean radius and how sampling of the line light curve and variability of the continuum light curve affect its measurement. Second, we consider the combination of the CCF lag with measurements of the emission line width to explore the uncertainty in black hole masses measured using the virial product.

4.1 Comparing the time lag and mean radius

One of the main assumptions in the traditional analysis is that the time lag measured from CCF analysis is related to some characteristic radius of the BLR. We explore the validity of this assumption by comparing the mean radius and the mean time lag in our geometry model of the BLR. We hold the mean radius fixed at $\mu = 4$ light days and allow the other geometry model parameter values to sample their priors as listed in Table 1, with the exception of the inclination angle, which we constrain to vary between zero (face-on) and 45 degrees. The results of this comparison are shown in Figure 8 for 200,000 samples. The difference between the mean radius, r_{mean} , and the mean lag, τ , is generally greater than one, meaning that the mean lag (in days) is usually shorter than the mean radius (in light days). This is due to the geometry parameter ξ that allows the midplane of the BLR to be transparent or opaque, since a BLR midplane that is not transparent will result in fewer particles with longer lags and hence a tendency for the mean lag to be smaller than the mean radius. The mean of $r_{\text{mean}} - \tau$ is 0.53 light days and the standard deviation of the distribution is 0.80 light days.

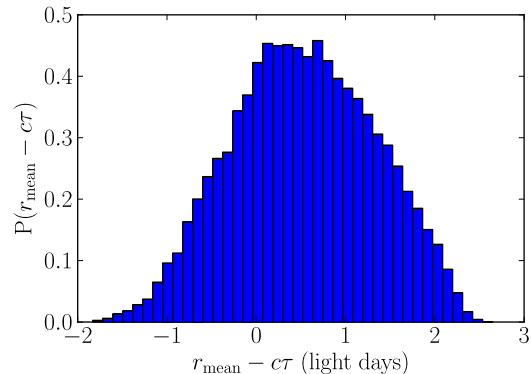


Figure 8. Difference between the mean radius and mean lag for BLR models drawn randomly from the prior with $\mu = 4$ light days. The distribution is asymmetric because the parameter ξ , the BLR plane transparency fraction, only shortens the mean lag compared to the mean radius, creating an excess of models where the mean radius is larger than the mean lag.

Table 4. Geometry model parameter values of simulated emission line light curves used in the comparison of direct modeling with the cross-correlation analysis approach.

Mock Line	τ_{mean} (days)	θ_i (deg)	θ_o (deg)	κ	β	F	ξ
1	3.69	10	25	-0.25	1.0	0.2	0.5
2	3.77	10	25	0.5	0.11	0.5	1
3	4.01	10	90	0.0	0.11	0.99	1
4	5.34	10	90	-0.5	0.11	0.99	1
5	4.00	0	0.5	0.0	0.11	0.99	1

All simulated datasets were created with a mean radius, μ , of 4 light days and with $\gamma = 1$.

This suggests that the uncertainty in using the time lag as a measurement of the mean radius is relatively small, on the order of the CCF time lag uncertainty typically quoted for high-quality reverberation mapping data of ~ 1 day.

4.2 The effects of line light curve sampling

Next we explore the dependence of the measured CCF lag on the geometry of the BLR and on the sampling characteristics of the emission line light curve. We focus on four very simple BLR geometries and one more realistic one, as shown in Figure 10, including

- (i) A nearly face-on wide disk with preferential emission from the far side and a disk midplane that is more than half opaque.
- (ii) A nearly face-on ring with preferential emission from the near side.
- (iii) A spherical shell (making a top-hat transfer function).
- (iv) A spherical shell with preferential emission from the far side.
- (v) A perfectly face-on thin ring (making a δ -function transfer function).

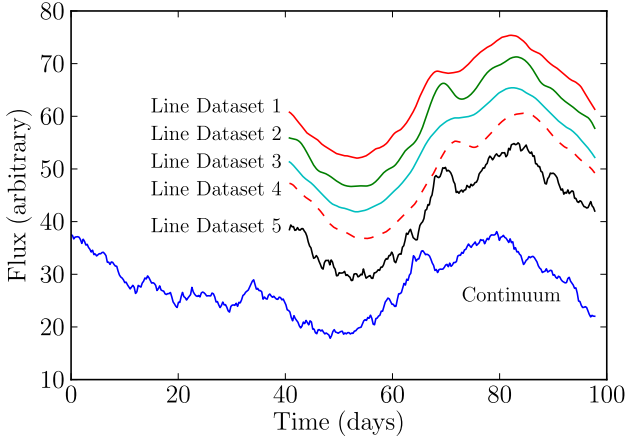


Figure 9. Simulated integrated emission line datasets including the AGN continuum light curve in solid blue and integrated $H\beta$ line light curves in solid red, green, cyan, black, and dashed red. The continuum light curve is based on the LAMP 2008 light curve of Arp 151 (Walsh et al. 2009). The simulated $H\beta$ line light curves correspond to five different BLR geometries, as shown in Figure 10.

We use these five geometries of the BLR to create simulated emission line light curves, as shown in Figure 9 using the same input continuum light curve and with very fine sampling of 0.1 days for both the line and continuum light curves. The geometry model parameter values are given in Table 4. In order to test how the quality of integrated emission line light curves affects measurement of the CCF lag, we degraded the quality of the simulated data by adding random Gaussian noise to the line light curve and by reducing the sampling cadence. For each simulated dataset degraded by adding σ_{noise} of random Gaussian noise, by sampling the line light curve at some fraction of the true mean radius of the BLR, and by losing a fraction of that sampled line light curve to weather, we computed the CCF lags τ_{cen} and τ_{peak} for 1000 realizations of assigning the random noise and losing a fraction of the light curve to weather. The simulated line light curves were degraded by:

(i) Reducing the sampling cadence to 1/10, 1/5, 1/3, or 1/2 of the true mean radius value of the geometry model of 4 light days. This means that the highest cadence is about half a day.

(ii) Adding random Gaussian noise, σ_{noise} , at the level of 0.05, 0.1, 0.2, 0.3, 0.4, 0.5, 0.6, 0.7, 0.8, 0.9, or 1.0 times the RMS variability of the simulated line light curve.

(iii) Including only a fraction of the total number of line light curve data points randomly from the light curve to simulate observations lost to weather. The fractions are 1, 3/4, 2/3, and 1/2.

Some illustrative results of this comparison are shown in Figure 11, with the lefthand column showing the CCF lag τ_{cen} versus the ratio of σ_{noise} over the RMS variability and with the righthand column showing the CCF lag τ_{cen} versus the cadence as a sampling fraction of r_{mean} . Figure 11 shows the results for when 3/4 of the line light curve is not lost to weather. The trend continues for larger fractions of the light curve lost to weather: the uncertainties on the mea-

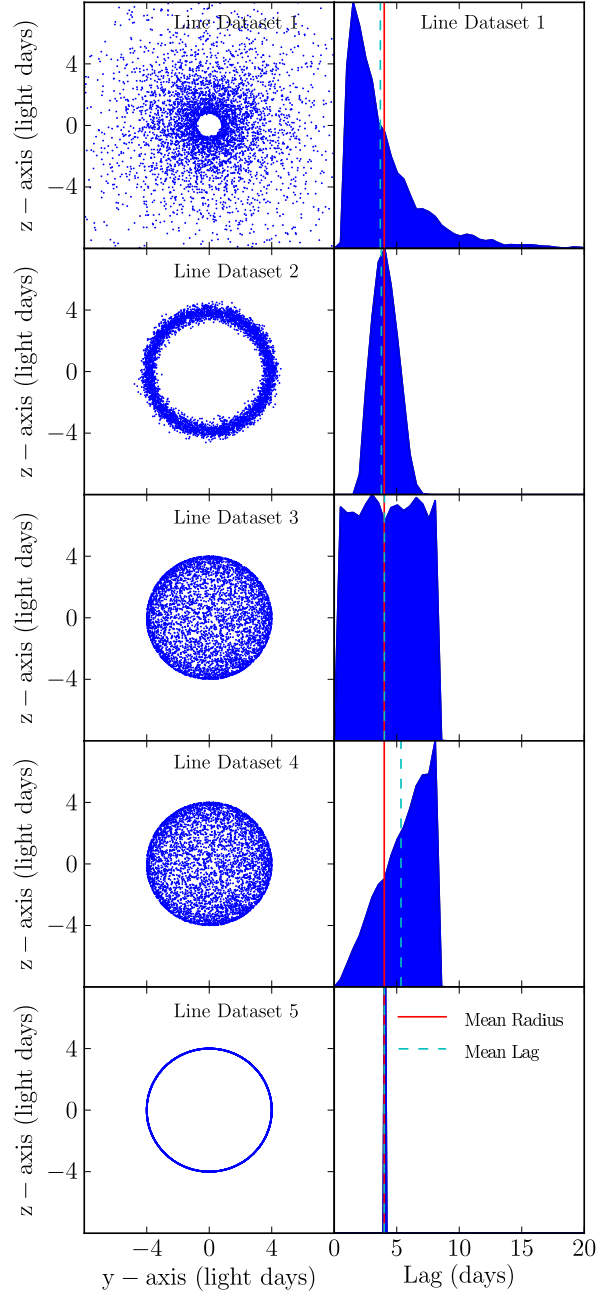


Figure 10. Geometries of the BLR (left panels) and corresponding transfer functions (right panels) of the simulated reverberation mapping datasets shown in Figure 9. Top to bottom BLR geometries: face-on wide disk, face-on donut, spherical shell, spherical shell with preferential emission from the back of the sphere, and a face-on thin ring.

sured CCF lag τ_{cen} increase while the mean lag measurement stays the same. For the case where no observations are lost to weather, the error bars become comparable to the size of the points in Figure 11. Overall, these results suggest that for different geometries of the BLR τ_{cen} can be offset from the true lag value by as much as a quarter of a light day (for a true mean lag of ~ 4 light days, see Table 4 for the exact values), which is well within typical uncertainties on CCF time lags quoted in the literature. For light curves with larger

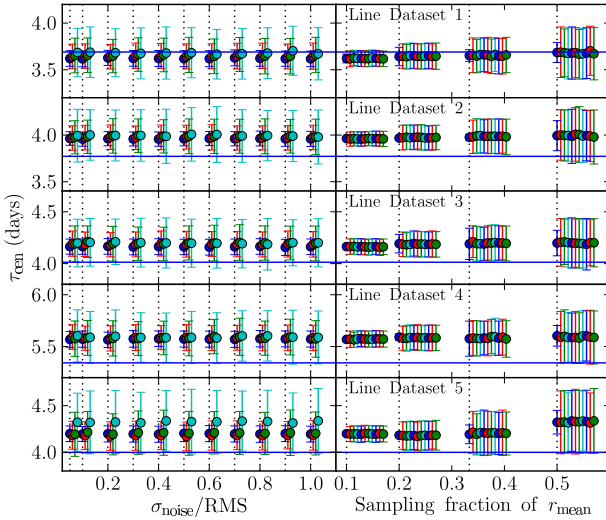


Figure 11. The CCF lag τ_{cen} as a function of the ratio of σ_{noise} to the RMS variability of the line light curve and versus the cadence as given by the sampling fraction of the mean radius. Top to bottom: simulated line dataset 1, 2, 3, 4, and 5. The horizontal blue lines show the true mean time lags for each simulated line dataset. The vertical dotted lines show the values of the x-axis for which each cluster of points correspond, where the clusters of points are spread out along the x-axis to show their spread. These results are for the case where 3/4 of the epochs are not lost to weather.

flux errors and lower cadence, this offset is easily within the error bars. In addition to a possible offset from the true lag values, these results show the importance of sampling the light curve at smaller fractions of the mean lag, even when the signal to noise quality of the light curve is high. As the fraction of the light curve lost to weather increases, this effect becomes more important. Detrending of the simulated light curves does not change these results.

4.3 The effects of continuum variability

In addition to light curve sampling effects, there is also the possibility that variability features in the AGN continuum light curve could affect measurement of CCF lags. We explore this source of uncertainty by generating 1000 random realizations of AGN continuum light curves, keeping the continuum hyper-parameters fixed to values similar to those inferred for Arp 151 and the BLR geometry model fixed to the values for simulated integrated line dataset 1 given in Table 4. Given each realization of the AGN continuum light curve and the fixed BLR geometry model, we generate an integrated emission line light curve. We use the sampling cadence of the LAMP 2008 dataset for Arp 151, described in Section 3.1, for each realization of the continuum and line light curves. We then calculate the CCF center-of-mass lag τ_{cen} for each of the 1000 realizations, obtaining successful CCF lag measurements for over 90% of the random continuum realizations.

The results are shown in Figure 12 as a histogram of τ_{cen} values, where we have truncated the histogram to between zero and fifteen days for clarity. The median and 68% confidence interval for all measurements of τ_{cen} is $3.33^{+1.33}_{-0.67}$

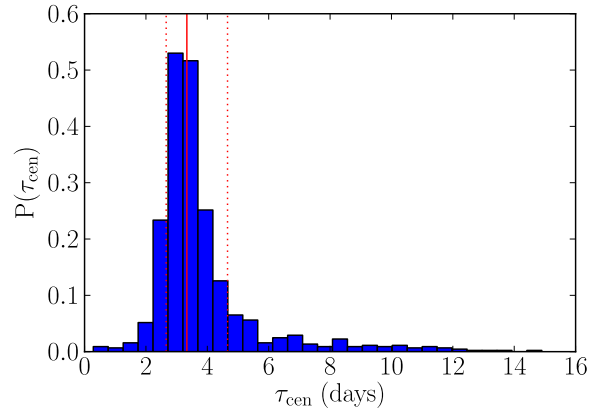


Figure 12. Histogram of the CCF center-of-mass time lag τ_{cen} for 1000 random continuum light curve model realizations. The true mean lag is 3.74 days. The vertical solid red line denotes the median value of 3.33 days and the dotted vertical red lines give the 68% confidence interval around the median at 2.66 and 4.66 days.

days, and considering only values of τ_{cen} between zero and fifteen days reduces the uncertainties by less than 0.1 days. Detrending of the simulated light curves results in a similar median value for τ_{cen} of $3.23^{+0.97}_{-0.61}$ days. These inferred median values for τ_{cen} agree to within the uncertainties with each other and the true value of the mean lag of 3.74 days. This test demonstrates that the main consequence of continuum variability is to add additional scatter to measurements of τ_{cen} on the order of ~ 1 day, without shifting the median measurement of τ_{cen} away from the true value.

4.4 Comparing the black hole mass and virial product

Other than the mean lag from CCF analysis, the black hole mass measured from the virial product is the key measurement of reverberation mapping studies. However the use of the virial product, $M_{\text{vir}} = c\tau\Delta v^2/G$, to measure black hole mass involves making many assumptions, including that the mean lag is a good measure of the physical scale of the BLR and that the width of the broad emission line is a good measure of the velocity field of the BLR. We attempt to quantify the uncertainty introduced by these assumptions by calculating the virial product from instances of our geometry and dynamics BLR model. We hold the black hole mass fixed at $M = 10^{6.5}M_{\odot}$ and the mean radius fixed at $\mu = 4$ light days while allowing all other geometry and dynamics model parameters to vary within their prior bounds, except for the inclination angle, which is limited to within zero (face-on) and 45 degrees. For each sample of a BLR model, we calculate the CCF lag τ_{cen} , the line dispersion of the RMS emission line profile, and the full width at half maximum (FWHM) of the mean line profile. Using these three values we can calculate the virial product either using the line dispersion or FWHM line width measurement. By further dividing the true black hole mass by the virial product we can work in terms of the virial coefficient f , where f_{σ} is calculated from the virial product using the line dispersion and f_{FWHM} is calculated from the virial product using the FWHM.

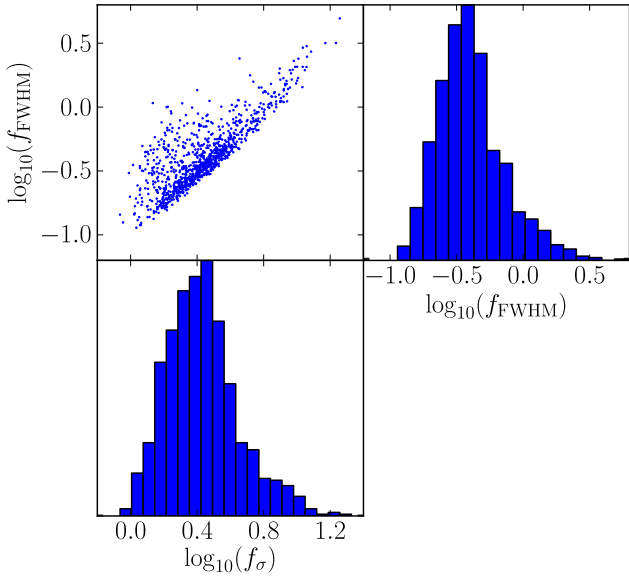


Figure 13. Distributions of f factor values for a fixed value of black hole mass and mean radius, with the other BLR model parameters allowed to vary. f_σ and f_{FWHM} are calculated using the CCF lag τ_{cen} and the line dispersion of the RMS emission line profile or the FWHM of the mean emission line profile respectively. The top left panel shows the correlation between f_σ and f_{FWHM} .

The results for the comparison of true black hole mass to virial product are shown in Figure 13 for 1000 samples of the BLR model parameters (other than M and μ , which are held fixed). The cadence of the continuum light curve and spectral time series were based on the cadence of the LAMP 2008 dataset for Arp 151, as described by Bentz et al. (2009). The values of $\log_{10}(f_\sigma)$ and $\log_{10}(f_{\text{FWHM}})$ are clearly correlated, but there is significant scatter in the relation. More importantly, the dispersion in the f factors is encouragingly small: the mean value of $\log_{10}(f_\sigma)$ is 0.43, with a standard deviation of 0.22, and the mean value of $\log_{10}(f_{\text{FWHM}})$ is -0.39 with a standard deviation of 0.26, where the dispersion in the f factors does not depend on whether the light curves have been detrended. This means that if the BLR is well described by our phenomenological model, we should not be surprised that the $M_{\text{BH}} - \sigma_*$ relation based on reverberation mapping black hole mass measurements does not have much larger scatter than the canonical ~ 0.4 dex found for galaxies with dynamical mass measurements.

5 CONCLUSIONS

In this paper we present an improved and expanded simply parameterized phenomenological model of the BLR for direct modeling of reverberation mapping data. In addition to describing the model in detail, we test the performance of the direct modeling approach using simulated reverberation mapping datasets with and without full spectral information. We also use this model of the BLR to explore sources of uncertainty in the traditional cross-correlation analysis used to measure time lags in reverberation mapped AGNs as well as sources of uncertainty in traditional measurements

of the black hole mass using the virial product. Our main conclusions are as follows:

(i) For simulated data with the same properties as the LAMP 2008 spectroscopic dataset for Arp 151, we can recover the black hole mass to within 0.05-0.25 dex uncertainty and distinguish between elliptical orbits and inflow. We recover the mean radius and mean lag with 5 – 12% uncertainties and the opening angle of the disk and inclination angle to within 5 – 10 degrees.

(ii) For the same simulated datasets, but where integrated emission line fluxes are used instead of the full spectroscopic information, we can use a BLR geometry model to constrain the mean radius and mean lag with 5 – 35% uncertainties and obtain only minimal constraints on the geometry of the BLR.

(iii) Using a combination of an integrated emission line light curve and a mean emission line profile for direct modeling allows for some constraints on the geometry of the BLR, but with greater uncertainty than from using the full spectroscopic dataset. The uncertainty in $\log_{10}(M_{\text{BH}}/M_\odot)$ is also greater compared to using the full spectroscopic dataset.

(iv) Comparison of BLR geometry modeling results to those from JAVELIN (Zu et al. 2011) and CCF analysis shows that JAVELIN recovers a time lag between the true mean and median lag, while CCF analysis recovers a time lag closer to the true mean lag. While the larger lag uncertainties from CCF analysis may reflect the unknown shape of the transfer function, the lag uncertainties from JAVELIN are smaller than the difference between the true mean and median time lag.

(v) By considering the range in possible BLR geometries of our model, we estimate the uncertainty in converting a mean lag into a mean radius to be $\sim 25\%$.

(vi) The CCF lag τ_{cen} can be offset from the true lag of a BLR model depending on the geometry. Both signal-to-noise of the flux light curve and sampling rate affect the dispersion in how far the CCF lag is relative to the true lag. Gaps in the light curve due to weather also introduce more uncertainty in the CCF lag.

(vii) For a given BLR geometry, changes in the variability features of the AGN continuum light curve introduces an uncertainty of $\sim 25\%$ into measurements of the CCF lag τ_{cen} .

(viii) By considering the range in possible BLR geometries and dynamics of our model, we estimate the uncertainty in measuring the black hole mass using the virial product to be smaller than the spread in the $M_{\text{BH}} - \sigma_*$ relation. We find that the standard deviation of $f = M_{\text{BH}}/M_{\text{vir}}$ is only ~ 0.25 dex, i.e. smaller than the uncertainty typically quoted for virial mass estimates.

The tests presented here demonstrate the unique capabilities of dynamical modeling of reverberation mapping data to constrain the geometric and kinematic properties of the BLR. While we can use hybrid datasets consisting of integrated line flux measurements and a mean emission line profile, considerably more information is available from modeling the reverberations across the emission line profile. The improvements we have made to this simply parameterized phenomenological model of the BLR have increased the flexibility of the method to fit a wider variety of emission line profiles. Future improvements will add a deeper con-

nection to photoionization physics, relating the distribution of broad line emission to the distribution of underlying gas, and explore the effects of non-gravitational forces, important for inferring the correct black hole mass.

These tests also confirm that the uncertainties inherent in the traditional analysis of measuring lags using the cross-correlation function and black hole masses using the virial product are relatively small, although larger than the formal uncertainties. The simplified problem of modeling integrated emission line light curves using a geometry-only model for the BLR presents an alternative approach for measuring time lags and mean radii of the BLR compared to the traditional analysis. One advantage to measuring time lags and mean radii with geometry modeling of the BLR is that the final uncertainties reflect the unknown underlying transfer function.

ACKNOWLEDGEMENTS

We would like to thank Aaron Barth, Mike Goad, Keith Horne, Daniel Proga, and Ying Zu for helpful discussions. AP acknowledges support from the NSF through the Graduate Research Fellowship Program. AP, BJB, and TT acknowledge support from the Packard Foundation through a Packard Fellowship to TT and support from the NSF through awards NSF-CAREER-0642621 and NSF-1108835. BJB is partially supported by the Marsden Fund (Royal Society of New Zealand).

APPENDIX A: COMPARISON OF DYNAMICS MODEL TO PREVIOUS WORK

In previous versions of our geometric and dynamical model of the BLR, we used a less general dynamical model in which point particle velocities were drawn from distributions of energy E and angular momentum L centered around the circular orbit energy and angular momentum values E_{circ} and L_{circ} (e.g. Pancoast et al. 2011; Brewer et al. 2011a; Pancoast et al. 2012). We can solve for E_{circ} by evaluating Equation 16 when $v_r = 0$ and $v_\phi = v_{\text{circ}}$:

$$E_{\text{circ}} = -\frac{1}{2} \frac{GM}{r}. \quad (\text{A1})$$

Similarly, we can solve Equation 16 for L , setting $v_r = 0$ and plugging in E_{circ} to find an expression for the angular momentum of a particle in a circular orbit:

$$L_{\text{circ}} = \sqrt{rGM}. \quad (\text{A2})$$

This previous E/L model incorporated inflow and outflow in the BLR gas through the fraction of elliptical orbits with positive or negative radial velocity component solutions. The inflowing and outflowing gas in the E/L model is thus always bound to the black hole.

For comparison to the current more general dynamical model in Figure A1, we show the distributions of energy and angular momentum in the $v_r - v_\phi$ plane for direct comparison with Figure 2. The radial and tangential velocity distributions for the E/L model are centered around the red dashed ring of radius v_{circ} and constrained to lie within the solid red circle, corresponding to orbits that are bound to the black hole. The velocity at which a particle

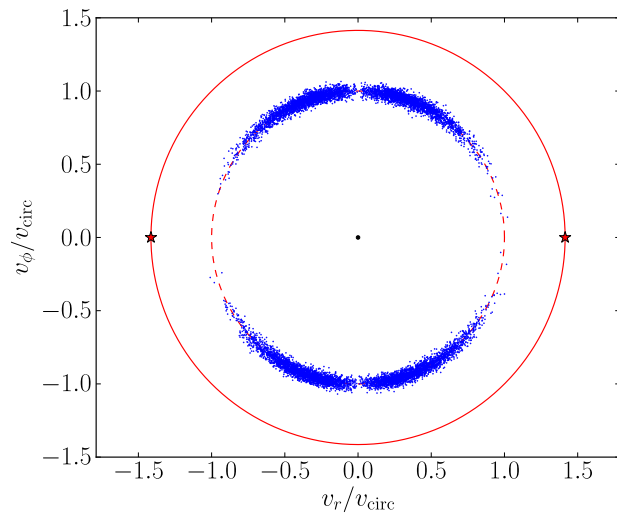


Figure A1. Distributions of radial and tangential velocities, v_r and v_ϕ for the previous E/L model. Blue points are particle velocities drawn from distributions in energy and angular momentum centered around the point for circular orbits $(v_r, v_\phi) = (0, v_{\text{circ}})$. Outflow corresponds to positive v_r . The outer solid red circle at a radius of $|v| = \sqrt{2GM/r}$ denotes the velocity beyond which orbits are unbound. The red dashed circle at a radius of $|v| = \sqrt{GM/r}$ denotes velocities with magnitude of the circular velocity and the circle around which bound elliptical orbits were distributed in the E/L model.

becomes unbound is given by setting $E = 0$ and solving for $|v| = \sqrt{v_r^2 + v_\phi^2} = \sqrt{2GM/r}$, which is $\sqrt{2}v_{\text{circ}}$. Unfortunately, while the distributions of E and L are centered around their circular orbit values, the chance of having a particle draw a close to circular orbit is vanishingly small, as shown by the lack of points in Figure A1 at $(v_r, v_\phi) = (0, v_{\text{circ}})$. This suggests a better way of including the circular orbit solution: draw point particle velocities directly from distributions in radial and tangential velocity space instead of in E and L space.

REFERENCES

- Antonucci, R. 1993, *ARA&A*, 31, 473
 Barth, A. J., Nguyen, M. L., Malkan, M. A., et al. 2011, *ApJ*, 732, 121
 Bentz, M. C., Peterson, B. M., Pogge, R. W., Vestergaard, M., & Onken, C. A. 2006, *ApJ*, 644, 133
 Bentz, M. C., Walsh, J. L., Barth, A. J., et al. 2009, *ApJ*, 705, 199
 Bentz, M. C., Denney, K. D., Grier, C. J., et al. 2013, *ApJ*, 767, 149
 Blandford, R. D., & McKee, C. F. 1982, *ApJ*, 255, 419
 Brewer, B. J., Pártay, L. B., & Csányi, G. 2011a, *Statistics and Computing*, 21, 649, *astrophysics Source Code Library*
 Brewer, B. J., Treu, T., Pancoast, A., et al. 2011b, *ApJL*, 733, L33
 Castor, J. I., Abbott, D. C., & Klein, R. I. 1975, *ApJ*, 195, 157

- Collier, S. J., Horne, K., Kaspi, S., et al. 1998, *ApJ*, 500, 162
- Collin, S., Kawaguchi, T., Peterson, B. M., & Vestergaard, M. 2006, *A&A*, 456, 75
- Denney, K. D., Peterson, B. M., Pogge, R. W., et al. 2010, *ApJ*, 721, 715
- Ferland, G. J., Korista, K. T., Verner, D. A., et al. 1998, *PASP*, 110, 761
- Ferland, G. J., Porter, R. L., van Hoof, P. A. M., et al. 2013, *RMXAA*, 49, 137
- Goad, M. R., Korista, K. T., & Ruff, A. J. 2012, *MNRAS*, 426, 3086
- Graham, A. W., Onken, C. A., Athanassoula, E., & Combes, F. 2011, *MNRAS*, 412, 2211
- Greene, J. E., Peng, C. Y., Kim, M., et al. 2010, *ApJ*, 721, 26
- Grier, C. J., Martini, P., Watson, L. C., et al. 2013a, *ApJ*, 773, 90
- Grier, C. J., Peterson, B. M., Horne, K., et al. 2013b, *ApJ*, 764, 47
- Horne, K. 1994, in *Astronomical Society of the Pacific Conference Series*, Vol. 69, *Reverberation Mapping of the Broad-Line Region in Active Galactic Nuclei*, ed. P. M. Gondhalekar, K. Horne, & B. M. Peterson, 23–25
- Horne, K., Welsh, W. F., & Peterson, B. M. 1991, *ApJL*, 367, L5
- Kaspi, S., Smith, P. S., Netzer, H., et al. 2000, *ApJ*, 533, 631
- Kelly, B. C., Bechtold, J., & Siemiginowska, A. 2009, *ApJ*, 698, 895
- Korista, K. T., & Goad, M. R. 2004, *ApJ*, 606, 749
- Korista, K. T., Alloin, D., Barr, P., et al. 1995, *ApJS*, 97, 285
- Kozłowski, S., Kochanek, C. S., Udalski, A., et al. 2010, *ApJ*, 708, 927
- Krolik, J. H., & Done, C. 1995, *ApJ*, 440, 166
- Li, Y.-R., Wang, J.-M., Ho, L. C., Du, P., & Bai, J.-M. 2013, *ApJ*, 779, 110
- Lynden-Bell, D., & Rees, M. J. 1971, *MNRAS*, 152, 461
- MacLeod, C. L., Ivezić, Ž., Kochanek, C. S., et al. 2010, *ApJ*, 721, 1014
- Marconi, A., Axon, D. J., Maiolino, R., et al. 2008, *ApJ*, 678, 693
- . 2009, *ApJL*, 698, L103
- Morgan, C. W., Kochanek, C. S., Morgan, N. D., & Falco, E. E. 2010, *ApJ*, 712, 1129
- Mushotzky, R. F., Edelson, R., Baumgartner, W., & Gandhi, P. 2011, *ApJL*, 743, L12
- Netzer, H. 2009, *ApJ*, 695, 793
- Netzer, H., & Marziani, P. 2010, *ApJ*, 724, 318
- Onken, C. A., Ferrarese, L., Merritt, D., et al. 2004, *ApJ*, 615, 645
- Pancoast, A., Brewer, B. J., & Treu, T. 2011, *ApJ*, 730, 139
- Pancoast, A., Brewer, B. J., Treu, T., et al. 2014, *MNRAS*, 445, 3073
- . 2012, *ApJ*, 754, 49
- Park, D., Kelly, B. C., Woo, J.-H., & Treu, T. 2012a, *ApJS*, 203, 6
- Park, D., Woo, J.-H., Treu, T., et al. 2012b, *ApJ*, 747, 30
- Peterson, B. M. 1993, *PASP*, 105, 247
- Peterson, B. M., Wanders, I., Horne, K., et al. 1998, *PASP*, 110, 660
- Peterson, B. M., Balonek, T. J., Barker, E. S., et al. 1991, *ApJ*, 368, 119
- Peterson, B. M., Ferrarese, L., Gilbert, K. M., et al. 2004, *ApJ*, 613, 682
- Peterson, B. M., Denney, K. D., De Rosa, G., et al. 2013, *ApJ*, 779, 109
- Proga, D. 1999, *MNRAS*, 304, 938
- Urry, C. M., & Padovani, P. 1995, *PASP*, 107, 803
- Walsh, J. L., Minezaki, T., Bentz, M. C., et al. 2009, *ApJS*, 185, 156
- Wandel, A., Peterson, B. M., & Malkan, M. A. 1999, *ApJ*, 526, 579
- Welsh, W. F. 1999, *PASP*, 111, 1347
- Whittle, M. 1992, *ApJS*, 79, 49
- Woo, J.-H., Schulze, A., Park, D., et al. 2013, *ApJ*, 772, 49
- Woo, J.-H., Treu, T., Barth, A. J., et al. 2010, *ApJ*, 716, 269
- Zu, Y., Kochanek, C. S., Kozłowski, S., & Udalski, A. 2013, *ApJ*, 765, 106
- Zu, Y., Kochanek, C. S., & Peterson, B. M. 2011, *ApJ*, 735, 80